Quaternary Science Reviews 322 (2023) 108419

Contents lists available at ScienceDirect

Quaternary Science Reviews

journal homepage: www.elsevier.com/locate/quascirev

The Holocene silicon biogeochemistry of Yellowstone Lake, USA

Petra Zahajská [a,b,c,*], Patrick J. Frings [d], François Gaspard [e], Sophie Opfergelt [e], Johanna Stadmark [a], Sherilyn C. Fritz [f], Rosine Cartier [a,g], Daniel J. Conley [a]

[a] Department of Geology, Lund University, Sölvegatan 12, 22362 Lund, Sweden
[b] Institute of Geography and Oeschger Center for Climate Change Research, University of Bern, Hallerstrasse 12, Bern, 3012, Switzerland
[c] Institute of Geology and Palaeontology, Faculty of Science, Charles University, Albertov 6, Prague, 12843, Czechia
[d] German Research Centre for Geosciences (GFZ), Section 3.3 Earth Surface Geochemistry, Telegrafenberg, Potsdam, 14473, Germany
[e] Earth and Life Institute, Université catholique de Louvain, Croix du Sud 2 bte L7.05.10 (De Serres B 213.10), Louvain–la–Neuve, 1348, Belgium
[f] Department of Earth and Atmospheric Sciences and School of Biological Sciences, University of Nebraska–Lincoln, Lincoln, NE 68588-0340, NE, USA
[g] CEREGE, Aix-en-Provence, France

ARTICLE INFO

Handling Editor: P. Rioual

Keywords:
Diatom
Silicon
Isotopes
Germanium
Yellowstone
Sediment
Lake
Holocene

ABSTRACT

Silicon (Si) is an essential macronutrient for diatoms, an important component of lacustrine primary productivity that represents a link between the carbon and silicon cycles. Reconstructions of lake silicon cycling thus provide an underexploited window onto lake and catchment biogeochemistry. Silicon isotope geochemistry has potential to provide these reconstructions, given the competing source and process controls can be deconvolved. The silica-rich volcanic and hydrothermal systems in Yellowstone National Park are a great source of dissolved silicon into Yellowstone Lake, a system with high silicon, and thus carbon, export rates and the formation of diatom–rich sediment. Yellowstone Lake sediments should be an archive of past silicon biogeochemistry, although the effect of sublacustrine hydrothermal activity or hydrothermal explosion events is unclear.

Here, we analysed lake water, tributaries, and hydrothermal vent fluids from Yellowstone Lake for their dissolved Si concentrations, isotope composition (δ^{30}Si) and Ge/Si ratios to evaluate the sources of variability in the lake's Si cycle. Bulk elemental composition and biogenic SiO_2 ($bSiO_2$) content, together with δ^{30}Si and Ge/Si ratios from a single diatom species, *Stephanodiscus yellowstonensis*, were analysed in two sediment cores spanning the last 9880 cal. yr BP. We investigate these datasets to identify long term Holocene changes in hydrothermal activity and effects of large and short-term events i.e., hydrothermal and a volcanic eruption.

Combinations of $bSiO_2$, δ^{30}Si and Ge/Si with XRF and lithology data revealed that Yellowstone Lake has a resilient biogeochemical system: hydrothermal explosions are visible in the lithology but have no identifiable impact on $bSiO_2$ accumulation or on the δ^{30}Si signature. Both cores show similarities that suggest a stable and homogeneous dSi source across the entire lake. A narrow range of δ^{30}Si and Ge/Si values suggests that the productive layer of the lake was well mixed and biogeochemically stable, with consistently high hydrothermal inputs of Si throughout the Holocene to buffer against the disturbance events. Variation in $bSiO_2$ concentration through time is weakly correlated with an increase towards younger sediment in the δ^{30}Si fossil diatom record in both cores. This increase mirrors that seen in ocean records, and follows changes known in summer insolation, summer temperatures and lake water-column mixing since the deglaciation. This suggests that climate forcing, and soil formation ultimately govern the silicon isotope record, which we suggest is via a combination of changes in weathering stoichiometry, diatom production, and relative proportion of dSi sources.

1. Introduction

The silicon cycle has extensively been studied for decades (Treguer et al., 1995; Tréguer et al., 2021; Tréguer and De La Rocha, 2013), motivated in part by the use of silicon isotope ratios (expressed as δ^{30}Si, the deviation in per mille of the $\frac{^{30}Si}{^{28}Si}$ ratio from the NBS-28 reference material) in diatom biogenic silica ($bSiO_2$) as a (palaeo)productivity proxy (e.g. De La Rocha et al., 1998). A long-term increase of 0.5 to 1.0‰ in diatom δ^{30}Si from the last glacial maximum (LGM, ca. 21 ka) to present is observed in many marine records (Sutton et al., 2018) and

* Corresponding author at: Institute of Geography and Oeschger Center for Climate Change Research, University of Bern, Hallerstrasse 12, Bern, 3012, Switzerland.
E-mail address: petra.zahajska@unibe.ch (P. Zahajská).

https://doi.org/10.1016/j.quascirev.2023.108419
Received 30 August 2023; Received in revised form 7 November 2023; Accepted 7 November 2023

is usually interpreted in terms of diatom Si utilisation (De La Rocha et al., 1998; Doering et al., 2019; Ehlert et al., 2013, 2015; Grasse et al., 2021; Hendry and Brzezinski, 2014). It has also been suggested that the records instead reflect whole-ocean changes in δ^{30}Si, which is ultimately driven by the continental weathering regime (Frings et al., 2016, 2021a; Opfergelt and Delmelle, 2012). These two endmember interpretations of the marine Si isotope record are not mutually exclusive, but whole-ocean changes should be quantified before inferences about productivity are made. However, identifying a whole-ocean change from marine records is challenging due to the long water residence time and the complexities added by ocean circulation. Lake sediments might be better suited to record millennial-scale changes in weathering regimes, as they typically offer an archive of catchment processes at higher temporal resolution with less internal buffering (e.g., Nantke et al., 2021; Street-Perrott et al., 2008). The inherent trade-off is a decrease in spatial scale, as lakes reflect local to regional signals (e.g., Opfergelt et al., 2011; Panizzo et al., 2018; Schmidtbauer et al., 2022). In this contribution, we use silicon isotope geochemistry to document the evolution of the silicon cycle in a hydrothermally influenced system, Yellowstone Lake (Wyoming, USA), and investigate its utility as a window onto lake and catchment dynamics.

Diatoms are important primary producers in Yellowstone Lake (Interlandi et al., 1999; Kilham et al., 1996). They have an obligate need for dissolved Si (dSi), and thus represent a key component of the lake silicon cycle. dSi is relatively enriched in Yellowstone Lake, with a mean concentration of ca. 200 μmol l^{-1} (Gemery-Hill et al., 2007) compared to a global river mean of 158 μmol l^{-1} (Dürr et al., 2011), a high-altitude alpine lakes range from 0 to 143 μmol l^{-1} (Mosello, 1984; Psenner, 1989), a USA lake mean of 143 μmol l^{-1} (Wang et al., 2016), or a global lake dSi mean of 19.6 μmol l^{-1} (Frings et al., 2014). The high dSi concentrations have two important implications: diatom production is conferred a competitive advantage relative to other algal groups, and the preservation efficiency of diatom frustules in the sediment is enhanced. The result is high sedimentary $bSiO_2$ content (up to 50 wt%) (Brown et al., 2021; Theriot et al., 2006) that provides an under-exploited siliceous archive of past environmental change.

Silicon isotope geochemistry is a powerful tool that utilises differences in the relative abundances of the three stable Si isotopes – ^{28}Si,^{29} Si and ^{30}Si – to trace the origin and fluxes of Si. The dSi released from primary minerals by interaction with meteoric water or hydrothermal fluids inherits the isotopic signature of the primary minerals from the rock. During uptake of dSi, both biosilicifiers and secondary mineral phase (e.g. clay) formation discriminate against the heavier silicon isotopes, which results in the residual solution being enriched in ^{30}Si relative to ^{28}Si (Cornelis et al., 2014; De La Rocha et al., 1997; Ziegler et al., 2005). The fractionation of silicon isotopes during biosilicification underpins the use of diatom δ^{30}Si as a palaeoproductivity proxy. Unfortunately, the direction and magnitude of fractionation by clay formation is similar, meaning the two processes cannot easily be distinguished with δ^{30}Si alone. This means an outstanding problem in the interpretation of diatom δ^{30}Si in lake and marine sediments is the extent to which it reflects changes of dSi sources versus diatom production (Opfergelt et al., 2011; Panizzo et al., 2017; Street-Perrott et al., 2008).

To add another constraint, the trace element germanium (Ge) can be used. Ge mimics the chemical behaviour of Si as it has a similar ionic radius and an identical outer electron structure, so it readily substitutes in Si-O bonds. Ge is thus considered to behave as a heavier 'pseudo'-isotope of Si (e.g. Froelich et al., 1992), though there are also important differences in geochemical behaviour of the two elements. As with Si, the ultimate source of dissolved Ge (dGe) is the weathering of primary silicate minerals (Frings et al., 2021b; Mortlock and Frohlich, 1987), and Ge and Si are fractionated relative to each other during most chemical and biological processes in a manner that may be complementary to δ^{30}Si (Froelich et al., 1989; Murnane and Stallard, 1988; Shemesh et al., 1989). Ge/Si ratios are typically elevated in hydrothermal fluids (e.g. Gaspard et al., 2021b,a), meaning they have particular potential to help disentangle source changes from biological processing in Yellowstone and similar environments.

As with the global ocean, we can conceptualize dSi inputs to Yellowstone Lake as predominantly coming from two sources: rivers and hydrothermal fluids. The burial of diatom frustules is the predominant dSi sink but (unlike the oceans) there is also a fraction of dSi that is exported in surface outflow. Here, we use the sediment record of Yellowstone Lake to investigate how the source and sink partitioning and endmember compositions vary over the Holocene. Yellowstone Lake has also experienced several large sub-lacustrine hydrothermal explosions during the Holocene that may have transient effects on lake Si cycling and sedimentary $bSiO_2$ concentration that have not yet been investigated. Focusing on the δ^{30}Si and Ge/Si ratios of diatom frustules, we demonstrate long-term trends that mirror those observed in marine records and are most easily explained by catchment weathering dynamics, but little evidence for impact of the hydrothermal explosions on lake functioning.

2. Study sites

Yellowstone Lake (YL) is located in north-western Wyoming, USA (44°29′N, 110°21′W) in Yellowstone National Park. The lake is at an elevation of 2358 m a.s.l. With a surface area of 341 km^2 and maximum depth of 131 m (Kaplinski, 1991), it is the largest high-altitude lake in North America (Morgan et al., 2003). The main lake basin is on the eastern margin of the Yellowstone Caldera, formed during the last cataclysmic eruption of the Yellowstone Plateau Volcanic Field at 0.64 Ma (Christiansen, 2001). The volcanism in Yellowstone National Park has a bimodal character, whereby both basic and acidic activity leads to the formation of andesites and rhyolites (Morgan et al., 2022; Morzel et al., 2017). The southern parts of the lake, shaped by glacial scour, are located outside of the caldera (Morgan et al., 2003). The Yellowstone Caldera rim divides the lake and its catchment into two different bedrock provinces. The north-western part of YL overlies rhyolitic post-caldera bedrock (Fig. 1, pink), whereas the south-eastern part is characterized mainly by Quaternary detrital deposits – silt, sand, gravel and till (Fig. 1, yellow), Quaternary rhyolitic ash-flow tuff (Fig. 1, orange) and Pleistocene rhyolite flow and andesitic alluvial facies with volcanic breccia (Fig. 1, grey).

Several large hydrothermal-explosion events have occurred in the lake in the last 15 ka, including the Mary Bay (13 ka) and Elliott's Crater (~ 8 ka) explosions (Fig. 1, Morgan et al., 2022; Morzel et al., 2017). Those explosions were sub-lacustrine eruptions accompanied with rapid ejection of boiling water, steam, sediment, mud and rock fragments from source craters (Browne and Lawless, 2001; Morgan et al., 2022; Muffler et al., 1971). The explosions were localized at the northern part of the lake and are recorded in the sedimentology and trace element geochemistry of the lake sediment (Morgan et al., 2022). The impact of those explosions on the lake system has been studied through diatom (Brown, 2019) and pollen (Schiller, 2020) assemblages, and oxygen isotope ratios of diatom silica, where all proxies show a limited response to the explosions (Brown et al., 2021). The largest hydrothermal explosions, such as Mary Bay, may have had an explosion column up to 1.9 km in height (Morgan et al., 2009, 2022). The deposits of Mary Bay explosion are distributed up to ~ 4 km from the crater rim and cover ~ 30 km^2, whereas the Elliot's Crater deposits extend ~ 0.8 km from the rim (Morgan et al., 2022).

The Yellowstone Lake region includes active fault systems and has continued active hydrothermalism (Morgan et al., 2007b). This hydrothermalism, driven by the interaction of meteoric water with mantle heat and volcanic gasses, influences the whole Yellowstone Caldera region (Hurwitz and Lowenstern, 2014) and occurs both within the lake and at well-known hydrothermal areas around the lake (Morgan et al., 2007a). The hydrothermal features in YL are caused by convective meteoric hydrothermal fluid circulation, steam separation during fluid ascent and possible CO_2 accumulation and release above an actively

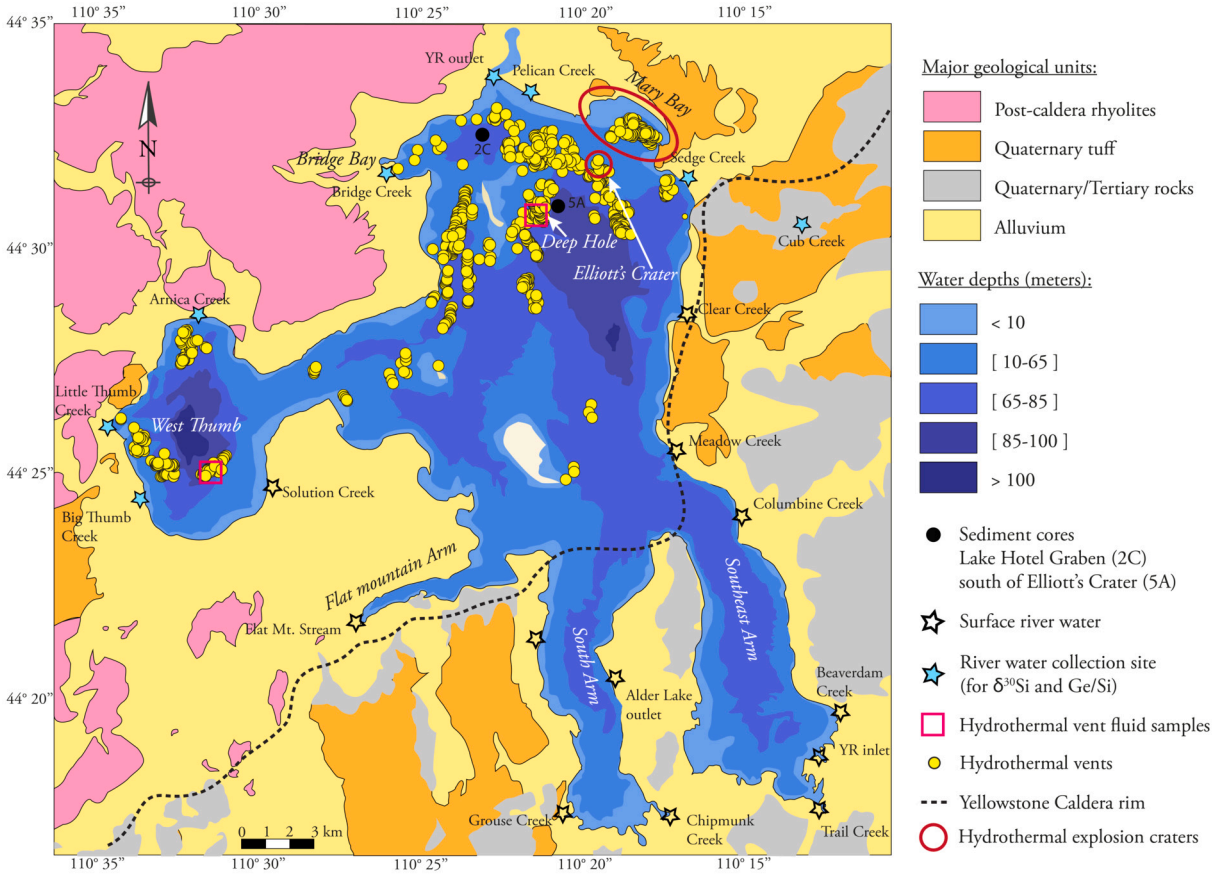

Fig. 1. A simplified geological map of Yellowstone Lake with lake bathymetry (modified from Morgan et al., 2007a). Sampling sites for sediment cores are marked as solid black circles, river samples as blue–filled stars, and hydrothermal vent fluids as pink squares. All unsampled major tributaries are shown as empty stars and mapped hydrothermal vents are shown as yellow circles. The dashed line defines the Yellowstone Caldera rim, where the north-west of Yellowstone Lake is in the Yellowstone Caldera.

degassing magma chamber (Morgan et al., 2007b). Hydrothermal fluids have high concentrations of dSi and other elements (Balistrieri et al., 2007; Fowler et al., 2019b), and the geochemical signature of those fluids is recognized in deposits surrounding the vents (Shanks et al., 2007; Tudor et al., 2021). Two types of hydrothermal vent field have been found within the lake. In the West Thumb area, the vents have a liquid form with a distinct elemental composition, enriched in Cl, Sb or W (Fowler et al., 2019b; Shanks et al., 2007), whereas in the Deep Hole area of the central basin, the character of the fluids is gaseous, with condensation at shallow depths and mixing with the lake bottom waters (Fowler et al., 2019a). Thus, Yellowstone Lake is enriched in various dissolved elements (e.g., As, B, Cl, Cs, Ge, Li, Mo, Sb) that originate from hydrothermal vent fluids. Elemental mass balances suggest that lake water is a mixture of 1% hydrothermal source fluid and 99% inflowing surface water (Balistrieri et al., 2007; Gemery-Hill et al., 2007).

Yellowstone Lake was glaciated until ca 14 ka. Since deglaciation, changes in summer insolation have produced variations in regional temperature and effective moisture that are reflected in diatom community shifts (Brown, 2019; Lu et al., 2017), endemic diatom species evolution (Theriot et al., 2006) fire history and vegetation shifts (Brown et al., 2021; Huerta et al., 2009; Iglesias et al., 2018; Millspaugh et al., 2000; Whitlock, 1993), and geochemical records (Whitlock et al., 2012). The region has a subarctic climate regime, influenced by Arctic and Pacific air masses in winter and by warm and moist Pacific air masses in summer (Despain, 1987). The watershed has been covered by coniferous forest for the last 9800 years, which has been disturbed by forest fires with a mean frequency of 2–5 fires per 1000 years (Millspaugh et al., 2000). The lake diatom community and the $\delta^{18}O$ stratigraphy indicate a progressive change towards cooler and wetter conditions during the Holocene that caused changes in lake stratification and nutrient inputs (Brown, 2019; Brown et al., 2021).

3. Methods

3.1. Sampling

Sediment cores YLAKE–YL16–2C–1K (hereafter '2C', taken at 61 m water depth, core length 11.62 m) and YLAKE–YL16–5A–1K ('5A', taken at 102 m water depth, core length 11.02 m) were collected with a Kullenberg sampler (Kelts et al., 1986) in 2016. Core 2C was retrieved from the deep basin at the north of the lake, and core 5A was located in proximity of Elliott's Crater (Fig. 1). Lithologic description (Morgan et al., 2022), subsampling, magnetic susceptibility (MS) measurements, and X–ray fluorescence core scanning (XRF) were done in the LacCore facility at the University of Minnesota. Subsampling of both cores was done at 8 cm intervals, and ~ 2 cm^3 of wet bulk sediment were sampled and freeze dried. MS was measured on both whole and split cores. XRF scanning was done at 0.5 cm resolution with 120 s scanning time with a Mo X–ray source at 30 kV and 15 mA to evaluate bulk sediment elemental (Al, Si, K, Ca, Ti, Fe, Rb, Sr, S, Mn, Zn, Zr, Cu, and As) composition.

Water samples from tributaries in the northern Yellowstone Lake watershed, situated within the Yellowstone Caldera and influenced by hydrothermal springs, were collected in August 2016 and June 2017 (Fig. 1). Tributaries from outside of the Yellowstone Caldera are not used in this study as they are not hydrothermally affected, and their dSi concentrations are lower than the lake dSi (Gemery-Hill et al., 2007). Sampling was conducted to constrain two different hydrological regimes – a low–flow regime at the end of the summer and a high–

flow regime during snowmelt (based on the Yellowstone River outlet hydrograph, USGS gauge station 443403110224801). All water samples were filtered through 0.45 μm Sterivex–HV Durapore filters and acidified in the field to pH 2 using HCl. Samples of hydrothermal fluids from the Deep Hole and the West Thumb vent fields (Fig. 1) were obtained as 25 times diluted solutions (see sampling details in Fowler et al., 2019b) from collaborators from the HD–YLake project, University of Minnesota, with dSi already measured by ICP-OES (Fowler et al., 2019b). Hydrothermal fluid samples with low dSi concentration were concentrated by MAGIC methodology following (Zhang et al., 2014). All water samples were purified by two–step ion–exchange chromatographic purification using anion-exchange resin (Biorad AG MP-1) and cation-exchange resin (Biorad AG50W-X12) for analyses of silicon isotope ratios (Gaspard et al., 2021b; Georg et al., 2006).

3.2. Chronology and accumulation rates

Sedimentation rates were derived from the published ^{14}C-based age-depth model (Morgan et al., 2022; Schiller et al., 2020b). The $bSiO_2$ accumulation rate (F_{bSiO_2}) was calculated from the sedimentation rates (SR), measured wet bulk density (ρ), porosity (Φ), which includes the information on sediment water content, and $bSiO_2$ weight percentages (see below) of dry sediment for each sample as:

$$F_{bSiO_2} = SR \cdot \rho \cdot (1 - \Phi) \cdot bSiO_2 wt\%. \quad (1)$$

Wet bulk density was obtained directly from the multi-scanner core logger (MSCL-XYZ) during the XRF scanning at LacCore facilities. Porosity was calculated from the bulk wet density and average particle density for diatomaceous sediments based on Niessen et al. (2013) and Geotek Limited manual (https://www.geotek.co.uk, accessed 2021).

3.3. Biogenic silica, total organic carbon, and dissolved silicon measurements

Sediment biogenic silica concentrations were analysed using a weak–alkaline extraction (40 ml of 0.1 M Na_2CO_3 at 85 °C in a shaking water-bath) of the bulk, freeze-dried, homogenized sediment (30 mg) adapted from Conley and Schelske (2001). The original protocol is premised on the idea that the $bSiO_2$ dissolves within the first 3 h of extraction, and so any subsequent increase in dSi concentration must reflect the (slower) dissolution of lithogenic silicates. The potential for silicon of non–biogenic origin to be released during the extraction was tested in a prolonged subsampling scheme up to 24 h (Clymans et al., 2015) for 12 samples, and demonstrated no resolvable increase in leachate dSi after 3 h. Thus, a mineral dissolution correction was not applied, and the estimates of $bSiO_2$ were simply calculated as the mean of aliquots taken at 3, 4 and 5 (6) hrs. All samples (n = 277) were analysed with two to four full chemical replicates. Previous experiments on tephra samples have shown that the possible contribution from volcanic glass to $bSiO_2$ concentration during the alkaline extraction ranges between 0.2 and 4% SiO_2 of the $bSiO_2$ (Clymans et al., 2015).

Total organic carbon (TOC) and total nitrogen content (TN) in the sediment were analysed using an elemental analyser (COSTECH ECS4010) at the Department of Geology, Lund University. Freeze-dried, homogenised samples (n = 74) were packed in tin capsules for TOC and TN analysis. All samples were analysed in duplicate. Additionally, 5 and 8 of TOC samples throughout cores 2C and 5A, respectively, were tested for carbonate content by a decalcifying procedure prior to the TOC measurement following Brodie et al. (2011).

All water samples were analysed for dSi concentrations using the automated molybdate–blue method (Strickland and Parsons, 1972) with a SmartChem 200, AMS System™ discrete analyser. The laboratory long-term external reproducibility based on regular in-house standard measurements of dSi concentration is within 4%, and the quantification limit is 0.28 $\mu mol \cdot l^{-1}$.

3.4. Preparation of diatoms for Si and Ge/Si analyses

Freeze-dried bulk sediment (2 cm^3 wet volume) was treated with H_2O_2 and HCl to remove organics and carbonates, respectively (Morley et al., 2004). Additionally, detrital particles were removed by heavy liquid density separation using sodium polytungstate (SPT) at a density range of 2.05 to 2.10 g $\cdot cm^{-3}$. The separated fraction was sieved through a 25 μm mesh. The residual fraction (below 25 μm) was filtered through 5 μm filter and archived. Final cleaning of the fraction above 25 μm from potentially adhered clay minerals was conducted by using 0.05 M sodium pyrophosphate for 0.5 to 24 h (with occasional shaking or sonication), and pure diatoms were obtained by another sieving at 25 μm. Sieving resulted in a near-monospecific *Stephanodiscus yellowstonensis* in the fraction >25 μm, and thus potential biases due to species specific fractionation are reduced. *S. yellowstonensis* is the only large centric diatom in the YL diatom community throughout the Holocene (Brown, 2019; Brown et al., 2021; Theriot et al., 2006) – the other centric diatoms (*S. minutulus*, *S. oregonicus*, *Aulacoseira subarctica*) are considerably smaller – hence we have achieved a single species sample for the further analyses. Diatom sample purity was visually confirmed using light and scanning electron microscope (Fig. S5), and the absence of mineral contamination was confirmed by energy dispersive spectroscopy (EDS) mapping, both on a Tescan Mira3 instrument at the Department of Geology, Lund University. A similar procedure was applied to hydrothermal deposits and Mazama ash layer samples, resulting in a cleaned mixture of diatoms and volcanic glass, which was further cleaned for Si isotope analysis.

Clean single species diatom samples (0.8–1.5 mg) were digested in 0.5 ml of 0.4 M NaOH (analytical purity) at 50 °C for at least 48 h in HDPE scintillation vials. After initial dissolution, samples were diluted with Milli-Q® water to lower dSi concentrations to prevent SiO_2 precipitation, and after 24 h they were neutralized by 0.4 M Suprapur® HCl. Before further sample processing, the silicon recovery was checked based on the initial individual sample amount mass and was between 66 to 100%. Recoveries below 95% reflect the effect of structural water in the biogenic silica structure (Jones and Handreck, 1967).

Diatom sample solutions were purified prior to stable Si isotope and Ge/Si analyses by ion-exchange chromatographic separation using 1.5 ml cation-exchange resin DOWEX® 50W-X8 (200–400 mesh) following Georg et al. (2006). The international Si standard NIST reference material RM-8-546 (NBS-28), secondary standard Diatomite (prepared by NaOH fusion after Georg et al. (2006)) and full procedural blanks were prepared using an identical protocol.

3.5. Stable silicon isotopes and Ge/Si analyses

The stable isotopes of purified water samples and *Stephanodiscus yellowstonensis* diatom samples (from core 2C and 5A) were measured on a NuPlasma (II) HR multi-collector inductively conducted plasma mass spectrometer (MC-ICP-MS, Nu Instruments™) with an Apex HF desolvating nebulizer at the Vegacenter, Swedish Museum of Natural History, Stockholm. Samples were checked for contamination by measuring the ^{28}Si signal of full procedural blanks that showed less than 0.35% of the total ^{28}Si signal. Samples were diluted to a dSi concentration of 71.5–107 $\mu mol \cdot l^{-1}$ and matrix matched with standards in 0.12 M SeaStar HCl. Further, all samples and standards were doped to contain 434 $\mu mol \cdot l^{-1}$ of Li (IPC-MS standard) to match the matrix of the Vegacenter standards (Sun et al., 2010). Stable Si isotope data are reported as deviations of $\frac{^{30}Si}{^{28}Si}$ and $\frac{^{29}Si}{^{28}Si}$ from the NBS-28 standard in per mil (‰), denoted δ^{30}Si and δ^{29}Si as follows:

$$\delta^{x}Si = \left(\frac{\left(\frac{^{x}Si}{^{28}Si}\right)_{sample}}{\left(\frac{^{x}Si}{^{28}Si}\right)_{NBS28}} - 1 \right) \cdot 1000, \quad (2)$$

where x is either 30 or 29. Each sample was measured three to four times in a single measurement session with a standard–sample–standard bracketing technique. Full chemical replicates were analysed for the majority of samples (n = 292, total measurements = 1875). Accuracy and reproducibility over three years on the secondary reference materials Diatomite ($\delta^{30}Si = 1.24 \pm 0.20‰$, 2SD, n = 285), Big-Batch ($\delta^{30}Si = -10.63 \pm 0.34‰$, 2SD, n = 109) and IRMM ($\delta^{30}Si = -1.77 \pm 0.22‰$, 2SD, n = 195) were in good agreement with values from a previous interlaboratory comparison (Reynolds et al., 2007). The repeatability of all samples was > 89%, thus the maximal absolute variation in $\delta^{30}Si$ between replicates was < 0.2‰). The absence of any potential polyatomic interferences was checked in a three-isotope plot of $\delta^{29}Si$ vs $\delta^{30}Si$, where all measurements fall onto a line that corresponds to a mass-dependent fractionation curve (Fig. S6).

Ge/Si analyses on the water samples were conducted at Université catholique Louvain-la-Neuve (UCL), Belgium. The Si concentrations in the thermal (n = 7) and river (n = 30) waters were determined by inductively coupled plasma optical emission spectrometry (ICP-OES; iCAP 6500 Thermo Fisher Scientific). The accuracy was assessed using the trueness (±4%) of the river water reference material SLRS-5 (Yeghicheyan et al., 2013) and the analytical precision (±0.5%) for each element. The detection limit was 0.36 $\mu mol \cdot l^{-1}$. The Ge concentration in the water samples was determined by ICP-mass spectrometry (ICP-MS, ICAPQ Thermo Fisher Scientific) using the ^{74}Ge isotope. Accuracy and long-term repeatability of the Ge analysis were assessed by measuring an international riverine standard, SLRS-5 ([Ge] = 0.083 ± 0.014 nmol $\cdot l^{-1}$; n = 3, published values 0.151 ± 0.151 nmol $\cdot l^{-1}$; Yeghicheyan et al. (2013) or SLRS-6 ([Ge] = 0.097 ± 0.0069 nmol $\cdot l^{-1}$; n = 3, published value 0.138 ± 0.096 nmol $\cdot l^{-1}$; Yeghicheyan et al. (2019)) in each analytical session. The limit of detection on Ge was 0.04 nmol $\cdot l^{-1}$, and the analytical precision (n = 3) was ± 8% for Ge concentrations < 0.013 nmol $\cdot l^{-1}$ and 4% for Ge concentrations > 0.013 nmol $\cdot l^{-1}$. The precision on the Ge/Si ratio is 10% (1SD).

Chromatographically (cation) purified solutions of dissolved diatom samples (from core 2C) were analysed for their Ge/Si ratios at GFZ Potsdam, Germany using an iCAP Q quadrupole ICP-MS (Thermo Fisher) following the protocol of Frings et al. (2021b). This approach exploits the recent demonstration that Ge is unfractionated relative to Si during the cation-exchange procedure used to purify Si from matrix elements for $\delta^{30}Si$ analyses (Delvigne et al., 2018). This means Si column elutants have a much cleaner matrix, which makes low Ge concentrations amenable to measurement by ICP–MS without the hydride generation and isotope-dilution protocols conventionally employed elsewhere (e.g., Kurtz et al., 2011). Samples were introduced in a 0.3 M HNO_3 matrix, via an ESI prepFast autodilutor system with the instrument operated under standard conditions. The measurement was based on 300 integrations of the isotopes of ^{74}Ge and ^{29}Si for 0.1 s, with the less abundant isotopes of Ge integrated 300 times for 0.01 s. Polyatomic interferences (e.g., ^{36}Ar, ^{38}Ar, on ^{74}Ge) were removed by a collision cell with He as reaction gas, at a flow rate of 5 ml $\cdot$ min^{-1}, yielding acid-blank counting statistics on ^{74}Ge < 1 cps. Beam intensities on the minor Ge isotopes correlate strongly with that of ^{74}Ge ($R^2 > 0.95$), corroborating the successful removal of unexpected isobaric or polyatomic interferences on ^{74}Ge by the column purification protocol and the instrument's collision cell. Ge/Si ratios were calculated directly from the ratio of beam intensities by reference to a set of gravimetrically prepared, matrix–matched calibration standards with matching Si concentrations but varying Ge concentrations. Thus, this approach does not directly yield Ge concentrations, because the column elutions are typically not performed gravimetrically, though these can be derived, if necessary, from pre-column Si concentration analyses. International silicate rock standards BIR-1 (Ge/Si = 2.72 ± 0.05 $\mu mol \cdot mol^{-1}$; 1SD, n = 16; expected range: 2.51-2.77 $\mu mol \cdot mol^{-1}$; Baronas et al. (2018); Kurtz et al. (2002); Mortlock and Froelich (1996); Mortlock and Frohlich (1987) and BHVO-2 (Ge/Si = 2.72 ± 0.13 $\mu mol \cdot mol^{-1}$; 1SD, n = 12; expected range: 2.45-2.7 $\mu mol \cdot mol^{-1}$; Delvigne et al. (2018); Jochum et al. (2005); Scribner et al. (2006) were measured in each analytical session to assess the accuracy and long-term repeatability of the Ge/Si analyses.

3.6. Numerical analyses

To understand the interplay of lithology, hydrothermalism and biological production, we examine selected proxies for correlations. Proxies for detrital input (XRF Ti and Zr counts, MS), hydrothermal and volcanic activity (XRF As and Cl counts, diatom Ge/Si ratios, total organic carbon (TOC) and diatom production and dissolution ($bSiO_2$, $\delta^{30}Si_{diatom}$) were tested for correlation was performed on both cores using Pearson correlation tests in the R Statistical Software (v4.1.2; R Core Team 2021). The significance of a correlation was evaluated through the *p*-value, using a threshold of 0.05 to assess significance, and the correlation reliability through the Pearson correlation coefficient R. We additionally examined linear regression models to test causality of selected correlations (Table 1, Supplementary Material). We do not aim to model any of our variables based on the regression models.

4. Results

4.1. Lithological, chemical, $\delta^{30}Si$ and Ge/Si composition of the sediment cores

The lithology of the two cores is described in (Morgan et al., 2022) where several lithological units originally defined by Tiller (1995) were identified and used for core alignment (Fig. 2). A sequence of the Elliot's crater hydrothermal explosion deposits is found in both cores. In core 2C these events are represented in a 5 cm-thick layer at depths 977 to 984 cm, whereas in core 5A those events are recorded in over 1 m-thick deposits from 805 cm to 937 cm (Morgan et al., 2022, pink shading in Fig. 2). The hydrothermal explosion deposits are inferred to occur at ~8000 cal. yr BP. Additionally, Mazama tephra is found at core depths 934 cm and 779 cm in core 2C and 5A, respectively. Increased XRF chlorine concentrations in the sediment are due to the character of the volcanic material (Fig. 2). The depletion of As in hydrothermal fluids due to loss during steam separation, adsorption by iron or co-precipitation with calcite (Stauffer and Thompson, 1984) compared to the water from the lake catchment can be used as an indicator of hydrothermalism in Yellowstone Lake (Morgan et al., 2022). Similar to As, the relatively higher concentrations of Sr in the tributaries and the lake water compared to the hydrothermal vent (Balistrieri et al., 2007; Gemery-Hill et al., 2007) means that more intensive hydrothermal activity in the lake will be manifested as lower sediment Sr concentrations (Morgan et al., 2022).

4.1.1. Core 2C

Core 2C shows relatively undisturbed sedimentation as recorded in MS and Ti data, which are somewhat positively correlated (*p*-value = $9.9 \cdot 10^{-4}$, R = 0.094) reflecting changes in detrital input (Figs. 2, S3, S5 & Table 1). In the relationship between Ti and MS we expect the MS being related to the detrital input. This correlation is significant, but not strong, likely due to the position of the core in the deep basin and the hydrothermal activity. We hypothesize that the hydrothermal activity signal may affect the MS signal and thus the Ti signal is not strongly related to MS. Ti is negatively correlated with As (*p*-value < $2.2 \cdot 10^{-16}$, R = −0.34), where As depletion suggests a hydrothermal input, since hydrothermal fluids are depleted in As compared to waters originating from the lake catchment. We test Ti and As to explore the sources of As. If the Ti and As would show strong relationship, As would be connected to detrital input. However, this is not the case (Table 1). Thus, Ti represents to detrital input and As the hydrothermal input, and these are rather independent of each other. A distinct peak in Cl at 934 cm is associated with the Mazama ash

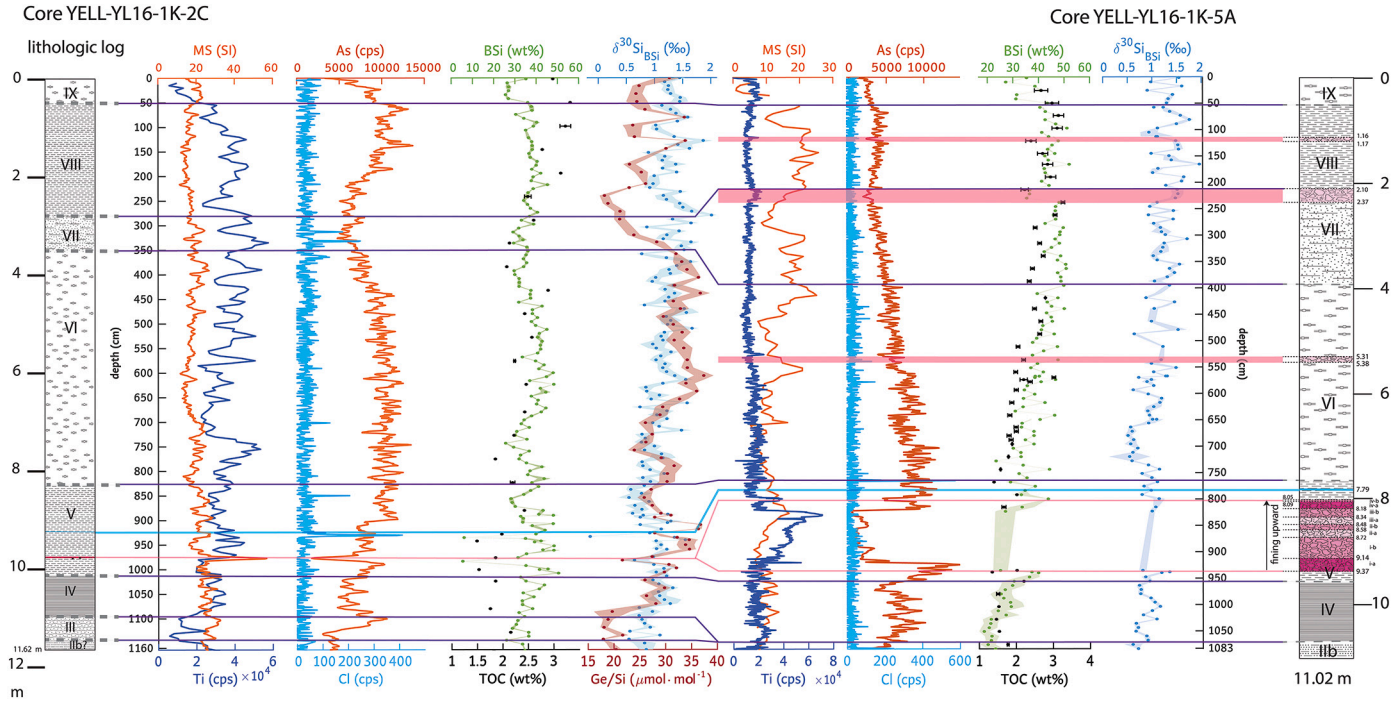

Fig. 2. Aligned cores 2C and 5A showing the lithological units (Morgan et al., 2022), magnetic susceptibility (MS), titanium (Ti) as proxy for detrital input, arsenic (As) and chloride (Cl); counts per second from XRF as proxy of hydrothermal activity (pink horizontal lines and zones) and tephra layers (blue horizontal line), biogenic silica ($bSiO_2$) in dry weight percentages SiO_2, total organic carbon (TOC) in dry weight percentages, stable silicon isotope ratios (δ^{30}Si, ‰) and Ge/Si ratios (μmol · mol^{-1}) of the single diatom species *Stephanodiscus yellowstonensis*.

tephra. Potassium (K) is strongly correlated with aluminium (Al) (p-value $< 2.2 \cdot 10^{-16}$, R = 0.91, Table 1), which may be connected with either autochthonous clay mineral formation induced by the hydrothermal activity at the lake bottom (Morgan et al., 2022) or increased detrital input as Al and K are positively correlated with Ti (Figs. S3 & S5).

Throughout the sediment sequence, the $bSiO_2$ concentration ranges from 25 wt% to 50 wt%, averaging 37 wt%. There is no pronounced trend in $bSiO_2$ concentration throughout the Holocene (p-value = 0.824), although variations in $bSiO_2$ concentration partly follow changes in As (Fig. 2, Table 1), a proxy for hydrothermal activity. A negative correlation and linear regression between $bSiO_2$ concentration and detrital input (Ti) (p-value $< 2.2 \cdot 10^{-14}$, R = −0.57) is consistent with dilution of $bSiO_2$ by increased detrital input. Al and K are both negatively correlated with $bSiO_2$ (p-value = $2.4 \cdot 10^{-8}$, R = −0.43, and p-value = $1.4 \cdot 10^{-12}$, R = −0.53, respectively), because of the inverse relationship between $bSiO_2$ concentration and detrital mineral concentrations. Total organic carbon (TOC) shows no significant correlation with $bSiO_2$ concentration, suggesting that TOC accumulation is not driven by total diatom production, but rather represents the total primary production, or that its variation is primarily controlled by other processes, such as organic matter inputs from the watershed, or preservation effects.

The Si isotopic composition of the diatom species *Stephanodiscus yellowstonensis* increases toward the top of the core, confirmed by negative correlation between δ^{30}Si and depth (p-value = $6.63 \cdot 10^{-12}$, R = −0.523). This trend is even more pronounced near the top of the core (0–50 cm), with a mean of 1.13±0.29‰ (1SD) (Fig. 2), with one standard deviation expressing the spread of data (total number of samples throughout the whole record n = 149). The lowest value of δ^{30}Si (0.53 ± 0.11‰, 2σ – analytical error) is in the bottom part of the core at depth of 852 cm, below the hydrothermal explosion deposits (Morgan et al., 2022). δ^{30}Si has a weak positive correlation with changes in $bSiO_2$ concentration (p-value = $2.2 \cdot 10^{-3}$, R = 0.25). We test the relationship between the biogenic silica and silicon isotopes, where in limited system, we expect to see positive relationship and strong correlation. Our regression shows (Table 1, Fig. S5), that only part of our data follows this trend and that in a relatively unlimited system, the isotopic values cannot be used to predict the BSi productivity completely. No obvious long-term impact of the hydrothermal events on δ^{30}Si in the vicinity of the deposits is observed.

The Ge/Si data measured on the fossil diatom *S. yellowstonensis* show extraordinarily high values, ranging from 17.9 to 37.4 μmol · mol^{-1}, with a mean Ge/Si ratio of 28.7 μmol · mol^{-1} (Fig. 2). The Ge/Si record has a lower resolution than the δ^{30}Si record, but nevertheless shows high variability throughout the core with no correlation with depth (p-value = 0.853). We examine the relationship between Si isotopes and Ge/Si where with increase Ge/Si as a proxy for hydrothermal activity we would expect lower isotopic values, as the Si source is lighter than then riverine Si source. This relationship is not seen, as probably both sources and maybe additional factors are determining the isotopic signature. However, the dependency of $bSiO_2$ on hydrothermal input (Ge/Si), which assumes that with increase hydrothermal input, there would be more silicon available for diatom to grow and for $bSiO_2$ to preserve in the sediment. This is nicely shown by the regression (Table 1, Fig. S5).

Although the Ge/Si ratios follow the As trends, there is only a weak positive correlation between Ge/Si and As (p-value = 0.0024, R = 0.30, see regression in Table 1). A negative correlation would show that the Ge/Si signal shows purely hydrothermal activity. Our Ge/Si values can be indeed partly explained by the hydrothermal activity, but also other source such as soil development in the lake watershed is probably responsible for the Ge/Si signal. Additionally, the hydrothermal activity proxy (As) shows no significant correlation with the δ^{30}Si record. All cross-correlation plots and regressions can be found in the Supplementary material, Figs. S3 & S5.

4.1.2. Core 5A

Core 5A reflects its proximity to the periphery of Elliot's Crater, best seen during the change in sedimentation between 805 to 937 cm, which

Table 1
Summary table of linear regression models of pre-selected elements from the correlation tests showing their relationship.

Core 2C	r	R^2	*p*-value	RMSEP	Linear regression equation	n
Ti∼MS	0.09	0.01	0.0015	8.4%	$y = 52.3x + 18482$	1154
Ti∼ $bSiO_2$	−0.57	0.32	$1.7 \cdot 10^{-14}$	14.4%	$y = -469.5x + 36416$	150
As∼Ti	−0.34	0.12	$2.5 \cdot 10^{-33}$	11.5%	$y = -0.16x + 11827$	1154
As∼Ge/Si	0.3	0.08	0.009	18.6%	$y = 163.6x + 4180$	77
K∼Al	0.91	0.82	0	3.7%	$y = 52.5x - 500$	1154
$bSiO_2 \sim \delta^{30}Si$	0.25	0.06	0.002	14.08%	$y = 5.2x + 30.5$	150
$bSiO_2$ ∼Ge/Si	0.45	0.1	$4.6 \cdot 10^{-5}$	13.6%	$y = 0.58x + 19.8$	77
Ge/Si∼ $\delta^{30}Si$	0.21	0.03	0.07	26.3%	$y = 3.5x + 24.6$	77
Core 5A	**r**	**R^2**	***p*-value**	**RMSEP**	**Linear regression equation**	**n**
Ti∼MS	0.55	0.3	$1.08 \cdot 10^{-173}$	11.9%	$y = 691x + 9664$	2200
Ti∼ $bSiO_2$	−0.72	0.51	$5.2 \cdot 10^{-20}$	14.8%	$y = -5393x + 21029$	118
$bSiO_2$ ∼TOC	0.69	0.47	$7.9 \cdot 10^{-8}$	20.1%	$y = 11.6x + 14$	47
$bSiO_2 \sim \delta^{30}Si$	0.51	0.26	$2.8 \cdot 10^{-9}$	22.1%	$y = 14.1x + 23.1$	118
$\delta^{30}Si$ ∼As	−0.47	0.22	$6.07 \cdot 10^{-8}$	19%	$y = -0.00006 + 1.43617$	118
As∼ $bSiO_2$	−0.38	0.14	$1.8 \cdot 10^{-5}$	17.5%	$y = -111x + 9990$	118

includes several hydrothermal deposits (Fig. 2), and also evident in the decreased As. MS and Ti, which are positively correlated (*p*-value = $7.3 \cdot 10^{-14}$, R = 0.55, Fig. S4) and represent changes in detrital input. We show though the linear regression of Ti and MS (Table 1 & Fig. S6), that the MS is related to the detrital input. This regression is significant, but not strong, however stronger than in the core 2C, thus position of core 5A probably records better the detrital input changes than the core in the deep basin. Both proxies increase in the hydrothermal deposits. Additionally, Ti is negatively correlated with As (*p*-value $< 2.2 \cdot 10^{-16}$, R = −0.27), which also suggests increased detrital input during hydrothermal activity (low As).

The $bSiO_2$ values in core 5A range from 18 wt% to 52 wt%, averaging 37 wt% throughout the Holocene (Fig. 2). A gradual increase in $bSiO_2$ content occurs towards the top (*p*-value $< 2.2 \cdot 10^{-16}$, R = −0.70). In unit VIII, the $bSiO_2$ concentration stabilizes, and in the topmost lithological unit IX $bSiO_2$ gradually decreases. The $bSiO_2$ record is negatively correlated with As (*p*-value = $1.5 \cdot 10^{-15}$, R = −0.38), which suggests that $bSiO_2$ variation can be connected to changes in hydrothermal inputs (As). This demonstrates the relationship between the diatom productivity and the hydrothermal input As. We expect to observe higher diatom productivity ($bSiO_2$) along with lower As as the higher hydrothermal input (lower As) would bring more silicon to the system. Similarly, we hypothesize that with higher biogenic silica there will be lower detrital input (Ti) due to the lower dilution. Ti is negatively correlated with $bSiO_2$ (*p*-value $< 2.2 \cdot 10^{-16}$, R = −0.72) with the detrital input diluting the accumulated $bSiO_2$, which is in an agreement with our hypothesis. At this site, $bSiO_2$ concentration is positively correlated with TOC content (*p*-value = $7.9 \cdot 10^{-8}$, R = 0.69, Table 1). The TOC is expected to be linked with the diatom production ($bSiO_2$). Thus, diatoms are a significant contributor to the total primary productivity.

As with core 2C, the *S. yellowstonensis* Si isotope record increases toward heavier $\delta^{30}Si$ throughout the core (*p*-value = $1.006 \cdot 10^{-13}$, R = −0.61), with a total shift of +0.6‰ (Figs. 2 & 4). Values range from 0.51 ± 0.06‰ (2σ – internal analytical) at 680 cm to 1.96 ± 0.07‰ (2σ) at 170 cm, with a mean of 1.09 ± 0.31‰ (1SD, n = 126). The $\delta^{30}Si$ is positively correlated with changes in $bSiO_2$ concentration (*p*-value = $5.8 \cdot 10^{-9}$, R = 0.54), which may indicate an effect of diatom production. We test the relationship between the biogenic silica and silicon isotopes, where in limited system, we expect to see positive relationship and strong correlation. Our regression shows that only part of our data follows this trend and that in a relatively unlimited system, like Yellowstone Lake, the isotopic values cannot be used to predict the $bSiO_2$ productivity completely. The $\delta^{30}Si$ and the $bSiO_2$ concentration show no long-term changes triggered by hydrothermalism. We also examine Si isotopes signal relationship with the hydrothermal proxy As. We expect with lower As to see lighter isotopic values, as the hydrothermal input is lighter Si isotope source compared to the riverine input. This is not the case, therefore, the $\delta^{30}Si$ show rather mixed signal of various sources and processes.

4.2. Chronology and accumulation rates of lake sediments

Diatom accumulation in the Yellowstone Lake sediment is quantified through mass accumulation rate calculations. The age–depth models of core 2C and 5A (Schiller et al., 2020b) produce mean sedimentation rates of $0.12\ cm \cdot yr^{-1}$ for the last 9800 years for core 2C, and of $0.11\ cm \cdot yr^{-1}$ for core 5A. Thus, the mean $bSiO_2$ accumulation rates for the whole cores are $8.01 \pm 2.76\ mg \cdot cm^{-2} \cdot yr^{-1}$ (1SD) for core 2C and $5.68 \pm 2.97\ mg \cdot cm^{-2} \cdot yr^{-1}$ (1SD) for core 5A. Since sedimentation rates in both cores are relatively constant, the $bSiO_2$ mass accumulation rates and $bSiO_2$ wt% can be used for interpretation interchangeably. However, we note the uncertainties of both age–depth models are large, with only 3 reliable ^{14}C dates for composite core 2C (11.62 m), one ^{14}C data for composite core 5A (11.02 m) and the Mazama ash layer available to construct the models (Morgan et al., 2022; Schiller et al., 2020b). Additionally, core 5A contains 1 m-thick hydrothermal explosion deposits, with no ^{14}C dates below those deposits; therefore, those numbers need to be interpreted with caution. Nevertheless, correlations between the cores are robust given the alignment of clearly identified lithological units (Section 4.1).

4.3. $\delta^{30}Si$ and Ge/Si ratios in tributaries and hydrothermal waters

All tributaries in the northern part of the lake, within the Yellowstone Caldera, show evidence of seasonality in flow (not shown), dSi concentrations, Ge/Si and $\delta^{30}Si$ (Table 2; Gaspard et al., 2021b). The $\delta^{30}Si$ of tributaries ranges from 0.37 ± 0.10‰ (σ internal analytical error) in the high–flow season to 1.19 ± 0.04‰ (σ) in the low-flow season, with an unweighted yearly mean of 0.65 ± 0.30‰ (1SD, n = 12) (Table 2). The Yellowstone River outlet, which we assume represents the Si isotope composition of the lake, has an annual mean $\delta^{30}Si$ of 1.94 ± 0.28‰ (1SD, n = 8) (Table 2).

Ge/Si ratios in Yellowstone Lake tributaries situated within the caldera show differences between the two flow regimes (Table 2; Gaspard et al., 2021b). The Ge/Si ratio ranges from 0.98 ± 0.20 $\mu mol \cdot mol^{-1}$ (2σ) in the high–flow regime to 11.35 ± 0.20 $\mu mol \cdot mol^{-1}$ (2σ) during the low–flow regime, with an annual mean of 4.26 ± 3.20 $\mu mol \cdot mol^{-1}$ (1SD, n = 12). This seasonal behaviour is also observed in the Yellowstone River outlet, where Ge/Si ranges from 13.6 ± 0.20 $\mu mol \cdot mol^{-1}$ (2σ) up to 23.3 $\mu mol \cdot mol^{-1}$, with the annual mean Ge/Si ratio of 18.8 ± 4.05 $\mu mol \cdot mol^{-1}$ (1SD, n = 8) (Table 2; Gaspard et al., 2021b).

Water samples of hydrothermal vents reflect two different vent systems in the lake: the fluid from the West Thumb vent field has isotopi-

Table 2
Data on tributaries and Yellowstone River outlet together with sublacustrine hydrothermal vents. dSi is dissolved silicon expressed as $\mu mol \cdot l^{-1}$, stable Si isotopic signature expressed as $\delta^{30}Si$ in per mille. Ge/Si ratio is expresses in $\mu mol \cdot mol^{-1}$. All Ge/Si data were measured at UCL, Belgium. The numbers of analytical replicates for dSi and $\delta^{30}Si$ are shown in column named *n*. Abbreviated 1SD represents standard deviation of several replicates and 1σ is the analytical error.

Yellowstone Lake tributaries in high-flow regime							
	dSi[c] $[\mu mol \cdot l^{-1}]$	1SD	$\delta^{30}Si$ [‰]	1σ	*n*	Ge/Si $[\mu mol \cdot mol^{-1}]$	1σ
Arnica Creek	657.08	117.67	0.37[L]	0.05	1	5.67	0.10
Big Thumb Creek	216.86	42.11	0.86[L]	0.02	1	0.88	0.10
Bridge Creek	741.13	104.19	0.71[L]	0.07	1	2.08	0.10
Little Thumb Creek	135.31	22.80	1.09[S]	0.11	5	0.98	0.10
Pelican Creek	458.52	15.81	0.78[L]	0.07	1	3.12	0.10
Sedge Creek	307.23	7.49	0.77[L]	0.05	1	6.02	0.10
Yellowstone River outlet	208.04	4.66	1.73[S]	0.08	3	18.21	0.10
			1.82[L]	0.04	1		
Yellowstone Lake tributaries in low-flow regime							
	dSi[c] $[\mu mol \cdot l^{-1}]$	1SD	$\delta^{30}Si$ [‰]	1σ	*n*	Ge/Si $[\mu mol \cdot mol^{-1}]$	1σ
Arnica Creek	968.31	35.45	0.40[L]	0.04	1	04.58	0.10
Big Thumb Creek	1675.48	61.58	1.19[L]	0.03	1	07.04	0.10
Bridge Creek	1530.35	54.92	0.48[L]	0.01	1	02.64	0.10
Little Thumb Creek	549.56	19.47	0.92[S]	0.06	4	01.47	0.10
Pelican Creek	1057.51	18.31	1.17[L]	0.06	1	08.95	0.10
Sedge Creek	584.84	33.45	1.05[L]	0.05	1	11.35	0.10
Yellowstone River outlet	194.89	2.50	2.05[S]	0.06	4	20.13	0.10
			2.17[L]	0.03	1		
	193.39	9.49	1.89[S]	0.09	10	23.29	0.10
			2.01[L]	0.09	2		
	214.70	31.62	1.45[S]	0.09	4	13.60	0.10
			1.63[L]	0.03	1		
West Thumb vent field							
	dSi[*] $[\mu mol \cdot l^{-1}]$	1SD	$\delta^{30}Si$ [‰]	1σ	*n*	Ge/Si $[\mu mol \cdot mol^{-1}]$	1σ
YL18F06	2597.35	< 10%	−0.32[P]	0.05	3		
YL18F12	4595.38	< 10%	−0.36[S]	0.05	3		
YL18F12			−0.32[S]	0.05	5		
YL18F12			−0.40[P]	0.05	3		
YL18F13	4495.52	< 10%	0.25[P]	0.08	2		
YL18F13			0.21[S]	0.01	3		
YL18F13			0.24[S]	0.08	3		
YL18F14	2697.21	< 10%	−0.15[P]	0.06	3		
Deep Hole vent field							
	dSi[*] $[\mu mol \cdot l^{-1}]$	1SD	$\delta^{30}Si$ [‰]	1σ	*n*	Ge/Si $[\mu mol \cdot mol^{-1}]$	1σ
YL16F06	539.41	< 10%	0.69[S]	0.08	3	10.87	0.10
YL16F06			0.62[P]	0.14	3		
YL16F07	229.84	< 10%	0.97[P]	0.15	3	25.54	0.10
YL16F10	389.62	< 10%	0.90[S]	0.08	3	11.20	0.10
YL16F12	449.53	< 10%	0.48[S]	0.03	3	12.74	0.10
YL16F12			0.49[S]	0.08	5		
YL16F14	539.41	< 10%	0.44[S]	0.08	3	14.61	0.10
YL16F14			0.41[P]	0.01	2		
YL17F01	419.58	< 10%	0.06[P]	0.09	3		
YL17F02	409.59	< 10%	0.11[P]	0.23	2		
YL17F03	429.56	< 10%	0.37[P]	0.14	3		
YL17F08	269.79	< 10%	1.10[P]	0.09	3		
YL18F02	419.58	< 10%	0.14[P]	0.10	3		
YL18F04	279.77	< 10%	0.84[P]	0.04	3		

[*] Concentrations measured by ICP-OES (Thermo Scientific iCAP 6500 duo) at the University of Minnesota (UMN), Department of Earth Sciences (Fowler et al., 2019b,a).
[c] Concentration measured by molybdate-blue spectrophotometry AMS SmartChem 200, Lund University, Sweden.
[S] Samples were measured by MC-ICP-MS (NuPlasma II) at Vegacenter, Swedish Museum of Natural history, Stockholm.
[P] Samples were measured on MC-ICP-MS (Neptune) at GFZ, Potsdam, Germany.
[L] Samples were measured by MC-ICP-MS (Neptune) at Université catholique Louvain-la-Neuve, Belgium.

cally lighter δ^{30}Si signatures with a mean δ^{30}Si of -0.11 ± 0.27‰ (1SD, n = 8), whereas the Deep Hole samples are isotopically heavier averaging at 0.54 ± 0.33‰ (1SD, n = 14), and have Ge/Si ratios as high as 25.5 $\mu mol \cdot mol^{-1}$ (Table 2).

5. Discussion

5.1. Source and sink partitioning in Yellowstone Lake

The silicon isotopic shifts in lake water and diatoms driven by dSi utilisation can be described by simple fractionation models underpinned by mass-balance (De La Rocha et al., 1997; Varela et al., 2004). In short, because diatom Si isotope fractionation discriminates against the heavier isotopes, with an isotope fractionation factor typically placed at around −1.1‰ (De La Rocha et al., 1997), the more dSi is utilized by diatoms, the more enriched in ^{30}Si the source solution becomes, and accordingly also the diatom frustules.

In Yellowstone Lake today, approximately 360 $Mmol \cdot dSi \cdot yr^{-1}$ enters the lake from rivers and from hydrothermal fluids, and approximately 230 $Mmol \cdot dSi \cdot yr^{-1}$ leaves the lake through the outflow to the Yellowstone River, based on the mass balance by Balistrieri et al. (2007) combined with our outlet dSi measurements. This implies a retention efficiency, f_{Si}, of 36%, or a burial rate of 23 $g \cdot m^{-2} \cdot yr^{-1}$ when distributed over the entire surface area of 341 km^2. This agrees reasonably well with our maxima of $bSiO_2$ mass accumulation rates (MAR) of 50-80 $g \cdot m^{-2} \cdot yr^{-1}$ in the deep basin, given the 'back-of-the-envelope' nature of the calculation and the lack of accounting for sediment focusing, such that we expect deeper parts of the lake to exhibit higher than average MAR. Isotope mass balance provides an independent estimate of dSi retention efficiency. Our best estimate of the mean inputs (including hydrothermal waters) of dSi to Yellowstone Lake have a δ^{30}Si value of +0.64‰, and the outlet has a δ^{30}Si value of +1.83‰. Assuming a diatom Si isotope fractionation factor of −1.1‰ implies a retention efficiency of >100% (calculated as retention $= (\frac{\delta^{30}Si_{in} - \delta^{30}Si_{out}}{\epsilon_{diatom}^{30/28}})$, implying the canonical diatom fractionation value of −1.1‰ (De La Rocha et al., 1998) might not be applicable to all freshwater systems (cf. Schmidtbauer et al., 2022). Reported diatom fractionations include values as low as −3.9‰, but even this extreme case would require at least 30% of inflowing dSi is retained within the lake. Thus, the Si isotopes also require a large lacustrine Si sink, regardless of the exact fractionation, in an agreement with the dSi mass-balance estimate. We can conclude that Yellowstone Lake – like most lakes (Frings et al., 2016) is an efficient Si scavenger.

5.2. Germanium as a complementary tracer to δ^{30}Si

Although Ge/Si ratios are arguably easier to measure, silicon isotope ratios have become the more established tracer of Si cycling. Nevertheless, Ge/Si ratios offer a powerful tool to probe Si biogeochemistry (Fernandez et al., 2021; Frings et al., 2021a). In particular, they can help test hypotheses about hydrothermal activity in Yellowstone and elsewhere, because hydrothermal end-members can have distinct Ge/Si signatures (Table 3, Fig. 3). Specifically, in Yellowstone, hydrothermal vent fluids often have high Ge/Si ratios, because of preferential uptake of Si into amorphous silica precipitates (Evans and Derry, 2002), which occurs due to dSi supersaturation of fluids during the contact with lake water and cooling (Fowler et al., 2019b; Shanks et al., 2007). When Si is incorporated in siliceous spires and precipitates, the residual solution is enriched in dGe and thus characterized by high Ge/Si ratios. Contrary to high-temperature dSi and dGe sources, low-temperature bedrock weathering produces Si-enriched solutions, resulting in low Ge/Si ratios (Baronas et al., 2018; Kurtz et al., 2011).

The mean Ge/Si ratios of world rivers range from 0.4 to 1.2 $\mu mol \cdot mol^{-1}$ (Baronas et al., 2018; Filippelli et al., 2000; Frings et al., 2021b; Froelich et al., 1992; Hammond et al., 2004; Mortlock and Frohlich, 1987). Marine hydrothermal fluids have higher Ge/Si ratios, at ca. 8 $\mu mol \cdot mol^{-1}$ to 14 $\mu mol \cdot mol^{-1}$ (Froelich et al., 1992; Sutton et al., 2010). The tributaries of Yellowstone Lake are mostly above the riverine mean, and some have Ge/Si values similar to marine hydrothermal fluids and higher, indicating a contribution from hydrothermal fluids (Gaspard et al., 2021b). Similarly elevated Ge/Si ratios have been observed in rivers of the Eastern Tibetan Plateau that have hydrothermal input (Evans and Derry, 2002; Han et al., 2015). The Deep Hole hydrothermal fluids (10.87-25.54 $\mu mol \cdot mol^{-1}$, Table 2), which may contain recycled Ge from the sediments or from diatom frustules, show even higher Ge/Si ratios than the tributaries (ranging from 0.88 to 1.35 $\mu mol \cdot mol^{-1}$, Table 2). Data from other rivers in the Greater Yellowstone area suggest that the waters from the whole region are highly enriched in Ge (Fig. 3; Gaspard et al., 2021b).

5.3. Long term trends in Yellowstone Lake Si isotope geochemistry

In two cores from Yellowstone Lake, we observe high and relatively stable $bSiO_2$ concentrations and fluxes. Interestingly, the long-term increase in the δ^{30}Si signature of *S. yellowstonensis* of +0.6‰ in both cores from early to late–Holocene is a pattern similar in direction and magnitude to that observed in marine records, where diatom production is driven by climate and nutrient supply by upwelling (Ehlert et al., 2013). At the same time, we see no systematic increase in diatom Ge/Si in core 5A. Yellowstone Lake has high dSi concentrations year-round and considering the back-of-the-envelope Si average retention compared to the burial rates from out $bSiO_2$ data (Section 5.1), there is no substantial effect of diatom dissolution below the water-sediment interface. Thus, in the simplest possible framework (Frings et al., 2021a; Nantke et al., 2021) three main factors can influence diatom δ^{30}Si and Ge/Si: the fractionation factor (or partition coefficient, for Ge/Si) associated with diatom Si uptake, the degree of dSi utilisation by diatoms, and the signature of the dSi source. Therefore, we explore several different non-exclusive scenarios to identify the factors responsible for variation in δ^{30}Si, Ge/Si, and $bSiO_2$ accumulation throughout the Holocene:

1. A variable silicon isotope fractionation and Ge/Si partitioning during Si uptake by diatoms;
2. The effect of dSi utilisation by diatoms;
3. The impact of changes in dSi sources:
   (a) Impact of hydrothermal explosions
   (b) Long-term shift in proportion of endmembers with constant composition
   (c) Constant proportions endmembers with changing δ^{30}Si composition.

5.3.1. A variable Si isotope fractionation factor and Ge/Si discrimination during Si uptake by diatoms

A possible explanation for variation in diatom δ^{30}Si is a variable Si isotope fractionation factor throughout the Holocene during Si uptake by diatoms. It is debated whether there is species specific Si fractionation (e.g., Meyerink et al., 2017, 2019; Sutton et al., 2013). Even if different taxa do have specific Si isotope fractionations, it is unlikely to contribute to the trends observed in our data given that the abundance of *S. yellowstonensis* remained stable over the entire record (Brown, 2019; Theriot et al., 2006). Nevertheless, there are indications that the same species can exhibit different fractionations in different environments (Meyerink et al., 2017; Schmidtbauer et al., 2022; Sutton et al., 2013). Both experiments and observations suggest this variability is independent of temperature and dSi concentrations (De La Rocha et al., 1997; Meyerink et al., 2019), but instead may reflect the availability of other micronutrients, such as iron (Meyerink et al., 2017; Schmidtbauer et al., 2022). We consider it unlikely but cannot fully rule out variation in the diatom fractionation factor: further studies on the δ^{30}Si of living diatoms and surface water are needed.

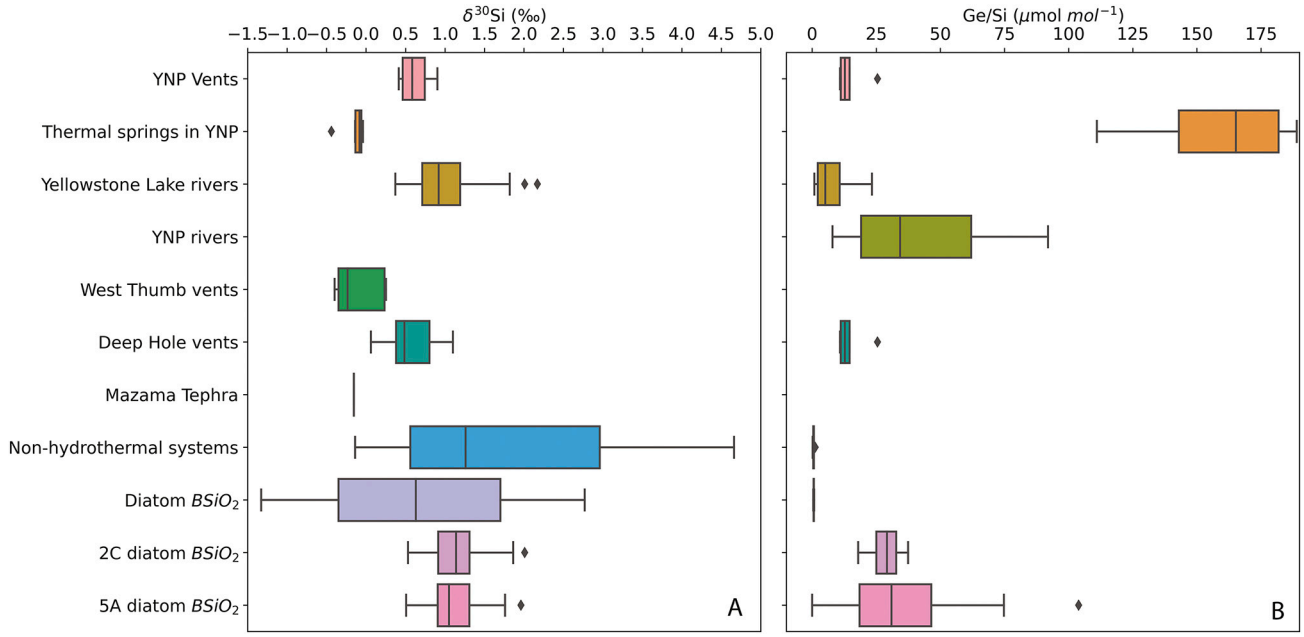

Fig. 3. (A) Ranges of stable silicon isotope ratios (δ^{30}Si) of Yellowstone Lake hydrothermal vent fluids and Yellowstone Lake tributaries, from thermal springs in Midway Geyser Basin (Gaspard et al., 2021b) and the range of δ^{30}Si found in the world's rivers (Frings et al., 2016; Sutton et al., 2018). In addition, the δ^{30}Si values of the Mazama ash layer, the ranges of fossil diatoms from core 2C and 5A and the world's marine and freshwater diatom δ^{30}Si ranges (Frings et al., 2016; Sutton et al., 2018, and references therein) are presented. (B) Ranges of Ge/Si ratios in the Deep Hole vent fluids, Yellowstone Lake tributaries and the fossil single species diatom opal from core 2C are shown. Further, the Ge/Si ratios in Greater Yellowstone rivers, Midway Geyser Basin thermal springs (Gaspard et al., 2021b) and ranges of world's Ge/Si ratios in non-hydrothermal systems and diatom opal (Froelich et al., 1992; Mortlock et al., 1991; Sutton et al., 2010) are presented.

The Ge/Si ratios of *S. yellowstonensis* are also much higher than typical values found in the literature (Fig. 3), which is consistent with the high Ge/Si ratio of source water. A handful of studies have examined uptake of dGe by marine diatoms (Azam et al., 1973; Froelich et al., 1989; Murnane and Stallard, 1988; Shemesh et al., 1989; Sutton et al., 2010) and have identified a general tendency for discrimination against Ge by diatoms, expressed as a distribution coefficient (KD) defined as $KD = \frac{Ge/Si_{diatom}}{Ge/Si_{solution}}$ (Froelich et al., 1989, 1992; Murnane and Stallard, 1988; Sutton et al., 2010). The KD ranges from 0.4 to 1.2, and Ge/Si ratios of diatoms typically range from 0.3 to 2.1 $\mu mol \cdot mol^{-1}$ (Froelich et al., 1992; Mortlock et al., 1991; Shemesh et al., 1989; Sutton et al., 2010; Tribovillard, 2013). Moreover, Ge uptake by diatoms was shown to be dependent on dSi concentration and the Ge/Si ratio in solution. Our high diatom Ge/Si values also require that *S. yellowstonensis* in Yellowstone Lake do not discriminate against Ge during uptake, otherwise we would never observe Ge/Si values of diatom frustules as high as 37 $\mu mol \cdot mol^{-1}$ formed in waters with maximum Ge/Si of 23 $\mu mol \cdot mol^{-1}$ (Table 2). This is consistent with the behaviour observed in diatom cultivation experiments using solutions with high Ge/Si ratios and dSi concentrations above 100 $\mu mol \cdot l^{-1}$, which yielded estimates of KD from 1 to 1.2 (Froelich et al., 1992). Thus, diatoms in YL likely do not discriminate against Ge during uptake, and perhaps even show a slight preference. A precise KD determination for YL would require lake water and living diatom Ge/Si measurements: enhanced knowledge of KD and detailed mass and isotope balances constraining all dSi and dGe sources and sinks would bring more clarity into the Yellowstone Lake Si and Ge cycling. Nevertheless, if we assume the KD to be constant through time and close to 1, then Ge/Si ratios in fossil diatoms are an archive of Ge/Si in the lake water through time.

5.3.2. The effect of dSi utilisation by diatoms

If the efficiency of diatom mediated burial of dSi has increased over the Holocene, this could be a driving mechanism behind the ca. 0.6‰ increases measured in cores 2C and 5A. This would be the conventional, palaeoproductivity focused interpretation of diatom δ^{30}Si as first outlined by De La Rocha et al. (1998): higher diatom production and burial results in greater relative dSi consumption and thus shifts the diatom δ^{30}Si signature towards heavier values in both cores. There are several lines of evidence that suggest this is not the full story.

First, the species we investigate here (*S. yellowstonensis*) has remained stable over the whole period we studied (Brown, 2019; Brown et al., 2021), implying no fundamental ecological shifts and thus no a priori reason to expect increased burial efficiency. Second, isotope mass balance provides strong constraints: an observed increase of 0.6‰ associated with a diatom burial flux that has a Si isotope fractionation of −1.1‰ implies a change in f_{Si}, the fraction of incoming dSi buried as $bSiO_2$, of 0.55. In other words, this implies at least a doubling of diatom productivity, if not burial. A utilisation-based interpretation of the Holocene δ^{30}Si trend would thus predict an increase in diatom $bSiO_2$ burial towards the present day, which is not observed. Indeed, the total range in $bSiO_2$ accumulation rates in all samples falls within a factor of two, which is insufficient to produce a Holocene increase of 0.6‰. Third, diatom production itself is not strongly temperature dependent (some of the most productive waters globally are in the Southern Ocean (Sutton et al., 2013)), and a Holocene temperature increase would be expected to decrease burial efficiency by increasing dissolution kinetics (cf. Westacott et al., 2021). This effect would be in the wrong direction. It is rather the changes in the lake mixing which have an impact on the $bSiO_2$ production, and thus burial. Finally, the diatom δ^{30}Si signature shows only weak positive correlation with $bSiO_2$ concentrations in both cores, and no correlation with TOC in core 2C. Overall, diatom production driven changes can have only a small influence on δ^{30}Si, implying that the prevailing factor driving the δ^{30}Si is changes in dSi sources.

5.3.3. Impact of changes in dSi sources

Impact of hydrothermal explosions We test the hypothesis of an impact of changes in dSi with hydrothermal explosions by tracking the sedimentary record around the hydrothermal events. Hydrothermal fluid composition is enriched in many elements, including dSi (Balistrieri et al., 2007; Fowler et al., 2019b). Nevertheless, as we show below, the hypothesis that hydrothermal explosions are visible in the $bSiO_2$ and δ^{30}Si records because of isotopically lighter dSi enrichment originating

from fluids brought by the explosion (Chen et al., 2020; De La Rocha et al., 2000; Ding et al., 1996; Douthitt, 1982; Geilert et al., 2014, 2015; Grasse et al., 2020; Opfergelt et al., 2011) is not supported by the data.

A series of hydrothermal explosion deposits occur in core 5A, and to a smaller extent in core 2C. Core 5A, located in proximity to Elliott's Crater, has a 1 m-thick hydrothermal deposit, yet no distinct increases in $bSiO_2$ accumulation nor a decrease in $\delta^{30}Si$ are observed in either of the cores above these deposits. Similarly, neither the $bSiO_2$ concentration nor the $\delta^{30}Si$ record changed directly after the explosion deposits in cores 2C or 5A. These observations can be explained by the lake dSi residence time (14 ± 3 years, Balistrieri et al., 2007) being too short to record short episodic explosions. Consistent with the geochemical data, only very subtle changes were found in the diatom community composition or in watershed vegetation (Brown, 2019; Brown et al., 2021; Schiller, 2020). As impacts of hydrothermal explosions could not be identified in either of the cores, the resolution of the $\delta^{30}Si$ sampling is not sufficient for identifying hydrothermal activity in a well–buffered environment with high dSi and several dSi sources imparting a similar isotopic signature.

Even though the Ge/Si ratios of fossil diatoms immediately above the explosion deposits hint at some increase in Ge concentrations (Fig. 2), it is not clear that the increase is connected to the hydrothermal event, because similar values are found higher up in the record. The consistent range of variation in Ge/Si supports the hypothesis of a relatively consistent long-term background of high hydrothermal inputs and the buffering capacity of the lake to these disturbances. Thus, even an extensive hydrothermal explosion, such as the Elliott's Crater event, had no observable impact on the lake Si cycle with respect to the dSi retention time. Comparing the recent lake Ge/Si and $\delta^{30}Si$ values suggests that Yellowstone Lake is greatly influenced by hydrothermalism, which created high Si and Ge background concentrations (Gaspard et al., 2021b, Fig. 3). Therefore, we do not see a great impact of the hydrothermal explosions on the $\delta^{30}Si$.

Long-term shift in proportion of endmembers with constant composition

Yellowstone Lake is highly influenced by hydrothermalism throughout the whole Holocene, such that the long-term trend in $bSiO_2$ accumulation and $\delta^{30}Si$ might reflect variation in the relative contribution of the dSi sources, which we simplify as the balance between vent fluids and river inputs. The mean $\delta^{30}Si$ signal of the tributaries situated within the Yellowstone Caldera (0.65 ± 0.30‰) is at the lower end of the world riverine $\delta^{30}Si$ range (Fig. 3). An isotopically lighter dSi source from hydrothermal vents (Fig. 3), is in agreement with existing data on hydrothermal vent fluids (Chen et al., 2020; Ding et al., 1996; Douthitt, 1982; Gaspard et al., 2021a; Geilert et al., 2014, 2015; Grasse et al., 2020; Opfergelt et al., 2011; De La Rocha et al., 2000) including hydrothermal vent fluids from West Thumb (Fig. 3, Table 3), which suggests that the vents in West Thumb can contribute to a lowering of the lake $\delta^{30}Si$. The Deep Hole hydrothermal fluids have previously been identified to be a mixture of lake water and pore water extruded by a vapour–driven hydrothermal system underlying the area (Fowler et al., 2019a), and the isotopic composition reflects those processes and is therefore closer to the lake $\delta^{30}Si$.

With knowledge of the Ge/Si and $\delta^{30}Si$ of the hydrothermal fluids, a relative change in the mixing ratio between hydrothermal dSi and riverine dSi sources can be one explanation for variation in $bSiO_2$ accumulation and the $\delta^{30}Si$ signature. The long-term increase toward heavier $\delta^{30}Si$ (Fig. 4) could be a response to a long-term decline of hydrothermal inputs relative to dSi brought in by tributaries, which carry heavier $\delta^{30}Si$ and lower Ge/Si resulting from pedogenesis. In support of this, a multiproxy palaeoclimate reconstruction from core 2C including both geochemical data and biotic proxies has shown a long-term trend towards cooler and wetter conditions during the Holocene (Brown et al., 2021). In particular, the late–Holocene was interpreted as a period with lower lake evaporation in a cooler climate, a conclusion based largely on oxygen isotope ratios in *S. yellowstonensis*. These oxygen isotope ratios are governed by a complex mix of climate, water source, precipitation regime and amount, and diatom ecology. While the oxygen isotope data (Brown et al., 2021) hint at possibly increased run-off – which would increase the fraction of relatively higher $\delta^{30}Si$, dSi and lower Ge/Si from the watershed soils – a conclusive interpretation is difficult. On the other hand, the diatom Ge/Si data, and the arsenic (As) data, both indicators of hydrothermal activity (Fig. 4), do not support a relative decline in hydrothermal activity. Nevertheless, water flow is only one term in the dSi flux – the other (river dSi concentration) might also change. Indeed, there is a substantial body of work suggesting that weathering rates are greatest in the early stages of soil development (e.g. Egli et al., 2001, 2003; Taylor and Blum, 1995; Zhou et al., 2016). The implication is that river dSi fluxes would have been higher in the post-deglaciation phase of catchment development. If the river dSi $\delta^{30}Si$ was similar to the modern value, then lake water $\delta^{30}Si$ would have also been higher, in contrast to observations (Table 3). Therefore, we infer an increasing contribution of catchment water inputs with a consistent delivery of dSi from hydrothermal water input, which is only a small component of the trend towards higher $\delta^{30}Si$ in Yellowstone Lake cores 2C and 5A.

Table 3
Estimated endmembers based on means of all measured water samples responsible for current lake $\delta^{30}Si$ and Ge/Si composition.

Estimated end-members	$\delta^{30}Si$ [‰]	1SD	Ge/Si [μmol · mol^{-1}]	1SD
Tributaries	0.65[L,S]	0.30	4.48[L]	3.21
West Thumb	−0.11[S,P]	0.27	–	–
Land springs	−0.14[L]	0.14	160[L]	26
Deep Hole	0.54[S,P]	0.33	15[L]	6
Lake	1.94[L,S]	0.28	18.8[L]	4.1

[L] Samples were measured by MC-ICP-MS (Neptune) at UCL, Belgium.
[S] Samples were measured by MC-ICP-MS (NuPlasma II) at Vegacenter, Swedish Museum of Natural history, Stockholm, Sweden.
[P] Samples were measured on MC-ICP-MS (Neptune) at GFZ, Potsdam, Germany.

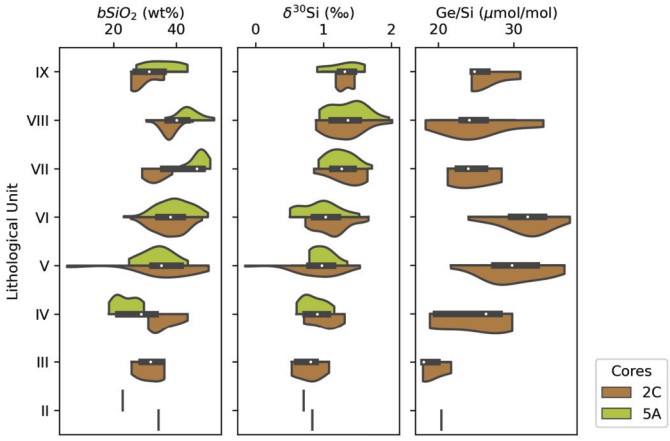

Fig. 4. Violin plots expressing $bSiO_2$ dry wt%, $\delta^{30}Si$ (‰) and Ge/Si (μmol · mol^{-1}) values (on x-axis) binned into lithological units (y-axis). The violin plot presents the data distributions of each core (2C in brown = lower half, 5A in green = upper half) for separate lithological units. The grey boxplot in between the data distributions shows the median computed from both datasets within the lithological unit (white circle), to demonstrate the general trend derived from both of the datasets, and the three quartile values of both cores data distribution (grey rectangle). This figure compares the data distribution of the two sediment cores: core 2C from the deep basin in the north of the lake, and core 5A at the distal part of Elliott's Crater, and reveals the lake signal by combining data from both coring locations.

Constant endmember proportions but changing δ^{30}Si composition A final explanation for the increase in diatom δ^{30}Si through the sediment record is that the proportion of dSi brought by tributaries and hydrothermal fluids remains stable though the Holocene, but the riverine endmember has shifted towards heavier isotopic signatures. Changes in δ^{30}Si towards heavier values can be caused by fractionation processes before and during the delivery into the lake. These processes include neoformation of secondary silicate minerals (i.e. clays and related phases), the incorporation of Si on to, or into, Fe- and Al-oxides, or plant uptake (Cornelis et al., 2011, 2014; Nantke et al., 2019; Struyf et al., 2010). We discount plant uptake as a major control, since the vegetation in the YL watershed has not changed substantively over this period: pollen records document only slight changes from a more open vegetation to a somewhat more forested landscape and the persistence of *Pinus* and *Artemisia* as dominant species (Schiller et al., 2022, 2020a). In any case, most Si taken up by plants is typically recycled within ecosystems (Carey and Fulweiler, 2012; Conley, 2002; Von Blanckenburg et al., 2021), such that there can be no net effect of river δ^{30}Si (Bouchez et al., 2013).

Instead, the trend towards heavier river δ^{30}Si could be a result of a net change in weathering reaction – i.e., the formation of relatively less depleted clays (e.g., smectites) towards the late-Holocene, with more kaolinite/allophane type clays in the early Holocene. Because smectite-group clay minerals tend to reflect more incongruent weathering reactions – i.e., a greater proportion of primary-silicate-hosted Si is retained in the new secondary phase – mass balance dictates the secondary phase must be isotopically close to the primary mineral. This means the dissolved Si counterpart can be offset from primary mineral δ^{30}Si. In contrast, more congruent weathering reactions – such as those that form kaolinite – release a greater fraction of the primary-silicate-hosted Si into solution, such that the solution must be close to the initial rock and the secondary phase is offset. We can thus read the Yellowstone Lake diatom δ^{30}Si record as reflecting the stoichiometry of weathering reactions in the catchment. A trend to more incongruent weathering reactions through time, following post-glacial exposure of bedrock to soil development, is largely consistent with glacial chronosequences in the Alps (Egli et al., 2003) and in Wyoming (Taylor and Blum, 1995).

Interestingly, the 0.6‰ increase in the Yellowstone Lake δ^{30}Si record is of a similar magnitude and direction as that seen in many ocean sediment records (see compilation in Frings et al., 2016). While acknowledging that YL is just one site, it demonstrates two important points for the interpretation of ocean δ^{30}Si records. First, we show that the δ^{30}Si of dSi delivered by rivers has likely substantially varied since the deglaciation. Though the ocean has a substantial buffering capacity due to its inventory of dSi, the dSi residence time (ca. 10 ka; Tréguer et al., 2021) is still short enough that millennial scale changes in input isotope composition should be recorded (cf. Richter and Turekian, 1993). Second, we demonstrate that changes in diatom productivity alone are unlikely to explain the observations: they are both implausibly large, and unsupported by independent lines of evidence (e.g., $bSiO_2$ burial rates). The Si cycle of Yellowstone Lake – and the growing number of palaeolimnological δ^{30}Si records (e.g. Chen et al., 2012; Cockerton et al., 2015; Nantke et al., 2021; Panizzo et al., 2016; Street-Perrott et al., 2008; Swann et al., 2010; Zahajská et al., 2021) – thus act as microcosms of the global ocean, with the benefit that detailed reconstructions of lake ecosystem and catchment soil development are much more amenable to study. We suggest that future work should expand the set of lake silicon isotope records to allow regional- to global-scale patterns to emerge.

6. Conclusions

The combination of recent water measurements and Holocene sedimentary data revealed that Yellowstone Lake has a stable water biogeochemistry over the long term, highly influenced by a large background hydrothermal input. An increase of 0.6‰ in δ^{30}Si in both cores over the Holocene, viewed in the context of interpretations of diatom assemblages from a previous multiproxy study at one of the sites (Brown et al., 2021), suggests an influence of climate on the δ^{30}Si records, likely via a change in the δ^{30}Si of dSi delivered by rivers. A change in the relative contributions of riverine to hydrothermal inputs to the lake may also have contributed to the observations, together with a slight increase in dSi utilisation by diatoms due to a longer period of spring mixing. Assuming constant hydrothermal fluid fluxes, increased river dSi inputs and/or higher river δ^{30}Si during the late–Holocene, is sufficient to explain the observed trends in δ^{30}Si.

Extreme hydrothermal events during the Holocene, such as during the formation of Elliott's Crater (Morzel et al., 2017) did not dramatically disrupt the lake system. The influence of hydrothermalism on the lake is apparent in recent water Ge/Si ratios. Continuous, long-term sublacustrine and terrestrial hydrothermal inputs govern the lake Ge/Si and Si isotope composition, which is reflected in extremely high Ge/Si ratios in fossil diatoms. However, a hydrothermal contribution following explosions events is not observed in the diatom δ^{30}Si, likely because of the large size of the lake with well mixed waters, the potential for other processes to mask the hydrothermal signature, and/or the alternation among dSi sources that share similar δ^{30}Si signatures.

The absence of evidence of increased $bSiO_2$, as an indicator of dSi, after the hydrothermal explosion deposits leads to the conclusion that either the hydrothermal explosion was vapour driven and disrupted sedimentation by clastics but did not contribute hydrothermal liquids or, alternatively, the impact of the explosion was buffered by the long lake residence time. The Ge/Si ratios in fossil diatoms reflect long-term changes in dSi and dGe sources and their proportion relative to the hydrothermal influence. The Ge/Si ratios of fossil diatoms compared to current lake tributaries and lake water Ge/Si ratios suggest that *Stephanodiscus yellowstonensis* fractionates Ge relative to Si, but positively, not negatively as expected. However, Ge/Si ratios could still be potentially used for tracking changes in Ge/Si ratios of lake water during the Holocene, once the extent of discrimination is known. Future work focused on Si and Ge budgets in lakes can contribute to a better understanding of the Si and Ge lacustrine sinks in volcanic systems, such as YL.

We have shown that the increase in diatom δ^{30}Si broadly mirrors the increase seen in ocean records. In the case of Yellowstone Lake, our analyses support the hypothesis that changes in the δ^{30}Si of diatom $bSiO_2$ may reflect primarily changes in the isotopic signature of the dSi delivered to the lake rather than changes in productivity.

CRediT authorship contribution statement

Petra Zahajská: Conceptualization, Data curation, Formal analysis, Funding acquisition, Investigation, Project administration, Resources, Visualization, Writing – original draft, Writing – review & editing. **Patrick J. Frings:** Conceptualization, Investigation, Methodology, Supervision, Writing – original draft, Writing – review & editing. **François Gaspard:** Investigation, Methodology, Writing – review & editing. **Sophie Opfergelt:** Conceptualization, Methodology, Supervision, Writing – review & editing. **Johanna Stadmark:** Conceptualization, Supervision, Writing – review & editing. **Sherilyn C. Fritz:** Conceptualization, Project administration, Resources, Supervision, Writing – review & editing. **Rosine Cartier:** Resources, Writing – review & editing. **Daniel J. Conley:** Conceptualization, Funding acquisition, Project administration, Resources, Supervision, Writing – review & editing.

Declaration of competing interest

The authors declare that they have no known competing financial interests or personal relationships that could have appeared to influence the work reported in this paper.

Data availability

Data will be available on PANGEA database.

Acknowledgements

This work was supported by The Royal Physiographic Society in Lund to PZ, RC, the Swedish Research Council to DJC, and NSF Grant No. 1515377 to SCF. DJC has received funding from the European Research Council (ERC) under the European Union's Horizon 2020 Research and Innovation Programme (Grant agreement No. 833454) and from the Knut and Alice Wallenberg Foundation. PZ was funded by The Charles University Grant Agency (GA UK), project No. 40217, supported by UNCE Center for Geosphere Dynamics, UNCE/SCI/006 and Swiss National Science Foundation grant 200020_204220. The research was conducted under Yellowstone National Park research permits YELL-2016–SCI–7018, YELL–2016–SCI–5054, YELL–2018–SCI–5054 and YELL–2018–SCI–7084. Yellowstone Lake coring was aided by M. Baker, C. Linder, R. O'Grady, M. Shapley, R. Sohn, and Yellowstone National Park rangers. LacCore provided coring infrastructure, laboratory space for core splitting, subsampling, and analyses including magnetic susceptibility. We also thank Lisa Morgan and Pat Shanks for assistance and help with core descriptions and lithological logs. Further we thank fieldwork participants Christopher Schiller, Jessica A. Eggers, Jacob Queen, Trisha Spanbauer and YNP rangers for their help. We acknowledge Hans Schöberg and Melanie Kielman for assistance during sample preparation and isotope data acquisition. This is Vegacenter contribution number # 070.

Appendix A. Supplementary material

Supplementary material related to this article can be found online at https://doi.org/10.1016/j.quascirev.2023.108419.

References

Azam, F., Hemmingsen, B.B., Volcani, B.E., 1973. Germanium incorporation into the silica of diatom cell walls. Arch. Microbiol. 92, 11–20. https://doi.org/10.1007/bf00409507.

Balistrieri, L.S., Shanks, W.C., Cuhel, R.L., Aguilar, C., Klump, J.V., 2007. The influence of sublacustrine hydrothermal vent fluids on the geochemistry of Yellowstone Lake. In: Publications of the US Geological Survey, pp. 1–30. https://digitalcommons.unl.edu/usgspubs/66.

Baronas, J.J., Torres, M.A., West, A.J., Rouxel, O., Georg, B., Bouchez, J., Gaillardet, J., Hammond, D.E., 2018. Ge and Si isotope signatures in rivers: a quantitative multi-proxy approach. Earth Planet. Sci. Lett. 503, 194–215. https://doi.org/10.1016/j.epsl.2018.09.022.

Bouchez, J., Von Blanckenburg, F., Schuessler, J.A., 2013. Modeling novel stable isotope ratios in the weathering zone. Am. J. Sci. 313, 267–308. https://doi.org/10.2475/04.2013.01.

Brodie, C.R., Casford, J.S., Lloyd, J.M., Leng, M.J., Heaton, T.H., Kendrick, C.P., Yongqiang, Z., 2011. Evidence for bias in C/N, δ^{13}C and δ^{15}N values of bulk organic matter, and on environmental interpretation, from a lake sedimentary sequence by pre-analysis acid treatment methods. Quat. Sci. Rev. 30, 3076–3087. https://doi.org/10.1016/j.quascirev.2011.07.003.

Brown, S., 2019. Diatom-inferred records of paleolimnological variability and continental hydrothermal activity in Yellowstone National Park, USA. PhD thesis. University of Nebraska. https://digitalcommons.unl.edu/geoscidiss/122.

Brown, S.R., Cartier, R., Schiller, C.M., Zahajská, P., Fritz, S.C., Morgan, L.A., Whitlock, C., Conley, D.J., Lacey, J.H., Leng, M.J., Shanks, W.P., 2021. Multi-proxy record of Holocene paleoenvironmental conditions from Yellowstone Lake, Wyoming, USA. Quat. Sci. Rev. 274, 107275. https://doi.org/10.1016/j.quascirev.2021.107275.

Browne, P., Lawless, J., 2001. Characteristics of hydrothermal eruptions, with examples from New Zealand and elsewhere. Earth-Sci. Rev. 52, 299–331. https://doi.org/10.1016/s0012-8252(00)00030-1.

Carey, J.C., Fulweiler, R.W., 2012. The Terrestrial Silica Pump. PLoS ONE, vol. 7, p. e52932.

Chen, J., Li, J., Tian, S., Kalugin, I., Darin, A., Xu, S., 2012. Silicon isotope composition of diatoms as a paleoenvironmental proxy in Lake Huguangyan, South China. J. Asian Earth Sci. 45, 268–274. https://doi.org/10.1016/j.jseaes.2011.11.010.

Chen, X.Y., Chafetz, H.S., Lapen, T.J., 2020. Silicon isotope variations in hydrothermal systems at Yellowstone National Park, Wyoming, USA. Geochim. Cosmochim. Acta 283, 184–200. https://doi.org/10.1016/j.gca.2020.06.004.

Christiansen, R.L., 2001. The Quaternary and Pliocene Yellowstone plateau volcanic field of Wyoming, Idaho, and Montana. Technical Report. URL https://pubs.er.usgs.gov/publication/pp729G.

Clymans, W., Barão, L., Van der Putten, N., Wastegård, S., Gísladóttir, G., Björck, S., Moine, B., Struyf, E., Conley, D., 2015. The contribution of tephra constituents during biogenic silica determination: implications for soil and paleoecological studies. Biogeosci. Discuss. 12, 3789–3804. https://doi.org/10.5194/bgd-12-3505-2015.

Cockerton, H.E., Street-Perrott, F.A., Barker, P.A., Leng, M.J., Sloane, H.J., Ficken, K.J., 2015. Orbital forcing of glacial/interglacial variations in chemical weathering and silicon cycling within the upper White Nile basin, East Africa: stable-isotope and biomarker evidence from Lakes Victoria and Edward. Quat. Sci. Rev. 130, 57–71. https://doi.org/10.1016/j.quascirev.2015.07.028.

Conley, D.J., 2002. Terrestrial ecosystems and the global biogeochemical silica cycle. Glob. Biogeochem. Cycles 16, 68. https://doi.org/10.1029/2002GB001894.1121.

Conley, J.D., Schelske, C., 2001. Biogenic silica. In: Tracking Environmental Change Using Lake Sediments, vol. 3. Springer, Netherlands, Dordrecht, pp. 281–293. chapter 14.

Cornelis, J.T., Titeux, H., Ranger, J., Delvaux, B., 2011. Identification and distribution of the readily soluble silicon pool in a temperate forest soil below three distinct tree species. Plant Soil 342, 369–378. https://doi.org/10.1007/s11104-010-0702-x.

Cornelis, J.T., Weis, D., Lavkulich, L., Vermeire, M.L., Delvaux, B., Barling, J., 2014. Silicon isotopes record dissolution and re-precipitation of pedogenic clay minerals in a podzolic soil chronosequence. Geoderma 235, 19–29. https://doi.org/10.1016/j.geoderma.2014.06.023.

De La Rocha, C., Brzezinski, M.A., DeNiro, M., Shemesh, A., 1998. Silicon-isotope composition of diatoms as an indicator of past oceanic change. Nature 395, 680–683. https://doi.org/10.1038/27174.

De La Rocha, C., Brzezinski, M.A., DeNiro, M.J., 2000. A first look at the distribution of the stable isotopes of silicon in natural waters. Geochim. Cosmochim. Acta 64, 2467–2477. https://doi.org/10.1016/s0016-7037(00)00373-2.

De La Rocha, C.L., Brzezinski, M.A., Deniro, M.J., 1997. Fractionation of silicon isotopes by marine diatoms during biogenic silica formation. Geochim. Cosmochim. Acta 61, 5051–5056. https://doi.org/10.1016/s0016-7037(97)00300-1.

Delvigne, C., Angeletti, B., Guihou, A., Basile-Doelsch, I., Meunier, J.D., 2018. Reliable determination of Ge in solid environmental samples using a chemical preparation procedure developed for Si isotopes and ICP-MS analysis. Geostand. Geoanal. Res. 42, 139–149. https://doi.org/10.1111/ggr.12197.

Despain, D.G., 1987. The two climates of Yellowstone National Park. In: Proceedings of the Montana Academy of Science, pp. 11–20.

Ding, T., Jiang, S., Wan, D., Li, Y., Li, J., Song, H., Liu, Z., Yao, X., 1996. Silicon Isotope Geochemistry. Geological Publishing House, Beijing.

Doering, K., Ehlert, C., Martinez, P., Frank, M., Schneider, R., 2019. Latitudinal variations in δ^{30}Si and δ^{15}N signatures along the Peruvian shelf: quantifying the effects of nutrient utilization versus denitrification over the past 600 years. Biogeosciences 16, 2163–2180. https://doi.org/10.5194/bg-16-2163-2019.

Douthitt, C.B., 1982. The geochemistry of the stable isotopes of silicon. Geochim. Cosmochim. Acta 46, 1449–1458. https://doi.org/10.1016/0016-7037(82)90278-2.

Dürr, H., Meybeck, M., Hartmann, J., Laruelle, G.G., Roubeix, V., 2011. Global spatial distribution of natural riverine silica inputs to the coastal zone. Biogeosciences 8, 597–620. https://doi.org/10.5194/bg-8-597-2011.

Egli, M., Fitze, P., Mirabella, A., 2001. Weathering and evolution of soils formed on granitic, glacial deposits: results from chronosequences of Swiss alpine environments. Catena 45, 19–47. https://doi.org/10.1016/S0341-8162(01)00138-2.

Egli, M., Mirabella, A., Sartori, G., Fitze, P., 2003. Weathering rates as a function of climate: results from a climosequence of the Val Genova (Trentino, Italian Alps). Geoderma 111, 99–121. https://doi.org/10.1016/S0016-7061(02)00256-2.

Ehlert, C., Grasse, P., Frank, M., 2013. Changes in silicate utilisation and upwelling intensity off Peru since the Last Glacial Maximum–insights from silicon and neodymium isotopes. Quat. Sci. Rev. 72, 18–35. https://doi.org/10.1016/j.quascirev.2013.04.013.

Ehlert, C., Grasse, P., Gutiérrez, D., Salvatteci, R., Frank, M., 2015. Nutrient utilisation and weathering inputs in the Peruvian upwelling region since the Little Ice Age. Clim. Past 11, 187–202. https://doi.org/10.5194/cp-11-187-2015.

Evans, M.J., Derry, L.A., 2002. Quartz control of high germanium/silicon ratios in geothermal waters. Geology 30, 1019–1022. https://doi.org/10.1130/0091-7613(2002)030<1019:qcohgs>2.0.co;2.

Fernandez, N.M., Perez-Fodich, A., Derry, L.A., Druhan, J.L., 2021. A first look at Ge/Si partitioning during amorphous silica precipitation: implications for Ge/Si as a tracer of fluid-silicate interactions. Geochim. Cosmochim. Acta 297, 158–178. https://doi.org/10.1016/j.gca.2021.01.007.

Filippelli, G.M., Carnahan, J.W., Derry, L.A., Kurtz, A., 2000. Terrestrial paleorecords of Ge/Si cycling derived from lake diatoms. Chem. Geol. 168, 9–26. https://doi.org/10.1016/s0009-2541(00)00185-6.

Fowler, A.P., Tan, C., Cino, C., Scheuermann, P., Volk, M.W., Shanks, W.P., Seyfried, W.E., 2019a. Vapor-driven sublacustrine vents in Yellowstone Lake, Wyoming, USA. Geology 47, 223–226. https://doi.org/10.1130/g45577.1.

Fowler, A.P., Tan, C., Luttrell, K., Tudor, A., Scheuermann, P., Shanks III, W.P., Seyfried Jr., W.E., 2019b. Geochemical heterogeneity of sublacustrine hydrothermal vents in Yellowstone Lake, Wyoming. J. Volcanol. Geotherm. Res. 386, 106677. https://doi.org/10.1016/j.jvolgeores.2019.106677.

Frings, P.J., Claymans, W., Fontorbe, G., Rocha, C.L.D.L., Conley, D.J., 2016. The continental Si cycle and its impact on the ocean Si isotope budget. Chem. Geol. 425, 12–36. https://doi.org/10.1016/j.chemgeo.2016.01.020.

Frings, P.J., Clymans, W., Jeppesen, E., Lauridsen, T.L., Struyf, E., Conley, D.J., 2014. Lack of steady-state in the global biogeochemical Si cycle: emerging evidence from lake Si sequestration. Biogeochemistry 117, 255–277. https://doi.org/10.1007/s10533-013-9944-z.

Frings, P.J., Oelze, M., Schubring, F., Frick, D.A., von Blanckenburg, F., 2021a. Interpreting silicon isotopes in the Critical Zone. Am. J. Sci. 321, 1164–1203. https://doi.org/10.2475/08.2021.02.

Frings, P.J., Schubring, F., Oelze, M., von Blanckenburg, F., 2021b. Quantifying biotic and abiotic Si fluxes in the Critical Zone with Ge/Si ratios along a gradient of erosion rates. Am. J. Sci. 321, 1204–1245. https://doi.org/10.2475/08.2021.03.

Froelich, P., Blanc, V., Mortlock, R., Chillrud, S., Dunstan, W., Udomkit, A., Peng, T.H., 1992. River fluxes of dissolved silica to the ocean were higher during glacials: Ge/Si in diatoms, rivers, and oceans. Paleoceanography 7, 739–767. https://doi.org/10.1029/92pa02090.

Froelich, P., Mortlock, R., Shemesh, A., 1989. Inorganic germanium and silica in the Indian Ocean: biological fractionation during (Ge/Si) opal formation. Glob. Biogeochem. Cycles 3, 79–88. https://doi.org/10.1029/gb003i001p00079.

Gaspard, F., Opfergelt, S., Dessert, C., Robert, V., Ameijeiras-Mariño, Y., Delmelle, P., 2021a. Imprint of chemical weathering and hydrothermalism on the Ge/Si ratio and Si isotope composition of rivers in a volcanic tropical island, Basse-Terre, Guadeloupe (French West Indies). Chem. Geol. 577, 120283. https://doi.org/10.1016/j.chemgeo.2021.120283.

Gaspard, F., Opfergelt, S., Hirst, C., Hurwitz, S., McCleskey, R.B., Zahajská, P., Conley, D.J., Delmelle, P., 2021b. Quantifying non-thermal silicate weathering using Ge/Si and Si isotopes in rivers draining the Yellowstone Plateau Volcanic Field, USA. Geochem. Geophys. Geosyst. 22. https://doi.org/10.1029/2021gc009904.

Geilert, S., Vroon, P.Z., van Bergen, M.J., 2014. Silicon isotopes and trace elements in chert record early Archean basin evolution. Chem. Geol. 386, 133–142. https://doi.org/10.1016/j.chemgeo.2014.07.027.

Geilert, S., Vroon, P.Z., Keller, N.S., Gudbrandsson, S., Stefánsson, A., van Bergen, M.J., 2015. Silicon isotope fractionation during silica precipitation from hot-spring waters: evidence from the Geysir geothermal field, Iceland. Geochim. Cosmochim. Acta 164, 403–427. https://doi.org/10.1016/j.gca.2015.05.043.

Gemery-Hill, P.A., Shanks, W.C., Balistrieri, L.S., Lee, G.K., 2007. Geochemical data for selected rivers, lake waters, hydrothermal vents, and subaerial geysers in Yellowstone National Park, Wyoming and vicinity. In: Publications of the US Geological Survey, pp. 1996–2004. https://digitalcommons.unl.edu/usgspubs/71.

Georg, R., Reynolds, B., Frank, M., Halliday, A., 2006. New sample preparation techniques for the determination of Si isotopic compositions using MC-ICPMS. Chem. Geol. 235, 95–104. https://doi.org/10.1016/j.chemgeo.2006.06.006.

Grasse, P., Closset, I., Jones, J., Geilert, S., Brzezinski, M., 2020. Controls on dissolved silicon isotopes along the US GEOTRACES Eastern Pacific Zonal Transect (GP16). Glob. Biogeochem. Cycles 34, e2020GB006538. https://doi.org/10.1029/2020gb006538.

Grasse, P., Haynert, K., Doering, K., Geilert, S., Jones, J.L., Brzezinski, M.A., Frank, M., 2021. Controls on the silicon isotope composition of diatoms in the Peruvian upwelling. Front. Mar. Sci. 8, 697400. https://doi.org/10.3389/fmars.2021.697400.

Hammond, D.E., McManus, J., Berelson, W.M., 2004. Oceanic germanium/silicon ratios: evaluation of the potential overprint of temperature on weathering signals. Paleoceanography 19, PA2016. https://doi.org/10.1029/2003pa000940.

Han, Y., Huh, Y., Derry, L., 2015. Ge/Si ratios indicating hydrothermal and sulfide weathering input to rivers of the Eastern Tibetan Plateau and Mt Baekdu. Chem. Geol. 410, 40–52. https://doi.org/10.1016/j.chemgeo.2015.06.001.

Hendry, K.R., Brzezinski, M.A., 2014. Using silicon isotopes to understand the role of the Southern Ocean in modern and ancient biogeochemistry and climate. Quat. Sci. Rev. 89, 13–26. https://doi.org/10.1016/j.quascirev.2014.01.019.

Huerta, M.A., Whitlock, C., Yale, J., 2009. Holocene vegetation–fire–climate linkages in northern Yellowstone National Park, USA. Palaeogeogr. Palaeoclimatol. Palaeoecol. 271, 170–181. https://doi.org/10.1016/j.palaeo.2008.10.015.

Hurwitz, S., Lowenstern, J.B., 2014. Dynamics of the Yellowstone hydrothermal system. Rev. Geophys. 52, 375–411. https://doi.org/10.1002/2014rg000452.

Iglesias, V., Whitlock, C., Krause, T.R., Baker, R.G., 2018. Past vegetation dynamics in the Yellowstone region highlight the vulnerability of mountain systems to climate change. J. Biogeogr. 45, 1768–1780. https://doi.org/10.1111/jbi.13364.

Interlandi, S.J., Kilham, S.S., Theriot, E.C., 1999. Responses of phytoplankton to varied resource availability in large lakes of the Greater Yellowstone Ecosystem. Limnol. Oceanogr. 44, 668–682. https://doi.org/10.4319/lo.1999.44.3.0668.

Jochum, K.P., Nohl, U., Herwig, K., Lammel, E., Stoll, B., Hofmann, A.W., 2005. GeoReM: a new geochemical database for reference materials and isotopic standards. Geostand. Geoanal. Res. 29, 333–338. https://doi.org/10.1111/j.1751-908X.2005.tb00904.x.

Jones, L., Handreck, K., 1967. Silica in soils, plants, and animals. Adv. Agron. 19, 107–149. https://doi.org/10.1016/S0065-2113(08)60734-8.

Kaplinski, M.A., 1991. Geomorphology and geology of Yellowstone Lake National Park, Wyoming. PhD thesis. Northern Arizona University.

Kelts, K., Briegel, U., Ghilardi, K., Hsu, K., 1986. The limnogeology-ETH coring system. Swiss J. Hydrol. 48, 104–115. https://doi.org/10.1007/bf02544119.

Kilham, S.S., Theriot, E.C., Fritz, S.C., 1996. Linking planktonic diatoms and climate change in the large lakes of the Yellowstone ecosystem using resource theory. Limnol. Oceanogr. 41, 1052–1062. https://doi.org/10.4319/lo.1996.41.5.1052.

Kurtz, A.C., Derry, L.A., Chadwick, O.A., 2002. Germanium-silicon fractionation in the weathering environment. Geochim. Cosmochim. Acta 66, 1525–1537. https://doi.org/10.1016/s0016-7037(01)00869-9.

Kurtz, A.C., Lugolobi, F., Salvucci, G., 2011. Germanium-silicon as a flow path tracer: application to the Rio Icacos watershed. Water Resour. Res. 47, W06516. https://doi.org/10.1029/2010wr009853.

Lu, Y., Stone, J., Fritz, S.C., Westover, K., 2017. Major climatic influences on Yellowstone-region lake ecosystems suggested by synchronous transitions in Late-Glacial and early-Holocene diatom assemblages. Palaeogeogr. Palaeoclimatol. Palaeoecol. 485, 178–188. https://doi.org/10.1016/j.palaeo.2017.06.011.

Meyerink, S., Ellwood, M.J., Maher, W.A., Strzepek, R., 2017. Iron availability influences silicon isotope fractionation in two Southern Ocean diatoms (Proboscia inermis and Eucampia antarctica) and a coastal diatom (Thalassiosira pseudonana). Front. Mar. Sci. 4, 217. https://doi.org/10.3389/fmars.2017.00217.

Meyerink, S.W., Boyd, P.W., Maher, W.A., Milne, A., Strzepek, R., Ellwood, M.J., 2019. Putting the silicon cycle in a bag: field and mesocosm observations of silicon isotope fractionation in subtropical waters east of New Zealand. Mar. Chem. 213, 1–12. https://doi.org/10.1016/j.marchem.2019.04.008.

Millspaugh, S.H., Whitlock, C., Bartlein, P.J., 2000. Variations in fire frequency and climate over the past 17 000 yr in central Yellowstone National Park. Geology 28, 211–214. https://doi.org/10.1130/0091-7613(2000)28<211:viffac>2.0.co;2.

Morgan, L., Shanks, W., Lee, G., Webring, M., 2007a. Bathymetry and geology of the floor of Yellowstone Lake National Park, Wyoming, Idaho, and Montana. Technical Report.

Morgan, L., Shanks, W., Pierce, K., Iverson, N., Schiller, C., Brown, S., Zahajska, P., Cartier, R., Cash, R., Best, J., Whitlock, C., Fritz, S., Benzel, W., Lowers, H., Lovalvo, D., Licciardi, J., 2022. The dynamic floor of Yellowstone, Lake, Wyoming, USA: the last 14 k.y. of hydrothermal explosions, venting, doming, and faulting. GSA Bull. https://doi.org/10.1130/b36190.1.

Morgan, L., Shanks, W.C., Lovalvo, D., Johnson, S., Stephenson, W., Pierce, K., Harlan, S., Finn, C., Lee, G., Webring, M., et al., 2003. Exploration and discovery in Yellowstone Lake: results from high-resolution sonar imaging, seismic reflection profiling, and submersible studies. J. Volcanol. Geotherm. Res. 122, 221–242. https://doi.org/10.1016/s0377-0273(02)00503-6.

Morgan, L.A., Shanks, W.C.P., Pierce, K.L., 2009. Hydrothermal Processes Above the Yellowstone Magam Chamber: Large Hydrothermal Systems and Large Hydrothermal Explosions, vol. 459. Geological Society of America.

Morgan, L.A., Shanks III, W.C., Pierce, K.L., Lovalvo, D.A., Lee, G.K., Webring, M.W., Stephenson, W.J., Johnson, S.Y., Harlan, S.S., Schulze, B., et al., 2007b. The floor of Yellowstone Lake is anything but quiet—New discoveries from high-resolution sonar imaging, seismic-reflection profiling, and submersible studies. Technical Report. URL https://digitalcommons.unl.edu/cgi/viewcontent.cgi?article=1076&context=usgspubs.

Morley, D.W., Leng, M.J., Mackay, A.W., Sloane, H.J., Rioual, P., Battarbee, R.W., 2004. Cleaning of lake sediment samples for diatom oxygen isotope analysis. J. Paleolimnol. 31, 391–401. https://doi.org/10.1023/B:JOPL.0000021854.70714.6b.

Mortlock, R., Charles, C., Froelich, P., Zibello, M., Saltzman, J., Hays, J., Burckle, L., 1991. Evidence for lower productivity in the Antarctic Ocean during the last glaciation. Nature 351, 220–223. https://doi.org/10.1038/351220a0.

Mortlock, R.A., Froelich, P., 1996. Determination of germanium by isotope dilution-hydride generation inductively coupled plasma mass spectrometry. Anal. Chim. Acta 332, 277–284. https://doi.org/10.1016/0003-2670(96)00230-9.

Mortlock, R.A., Frohlich, P.N., 1987. Continental weathering of germanium: Ge/Si in the global river discharge. Geochim. Cosmochim. Acta 51, 2075–2082. https://doi.org/10.1016/0016-7037(87)90257-2.

Morzel, L.A.M., Shanks, W.P., Lowenstern, J.B., Farrell, J.M., Robinson, J.E., 2017. Geologic field-trip guide to the volcanic and hydrothermal landscape of the Yellowstone Plateau. Technical Report.

Mosello, R., 1984. Hydrochemistry of high altitude alpine lakes. Schweiz. Z. Hydrol. 46, 86–99. https://doi.org/10.1007/bf02538100.

Muffler, L.P., White, D., Truesdell, A., 1971. Hydrothermal explosion craters in Yellowstone National Park. Geol. Soc. Am. Bull. 82, 723–740. https://doi.org/10.1130/0016-7606(1971)82[723:heciyn]2.0.co;2.

Murnane, R., Stallard, R., 1988. Germanium/silicon fractionation during biogenic opal formation. Paleoceanography 3, 461–469. https://doi.org/10.1029/pa003i004p00461.

Nantke, C.K., Brauer, A., Frings, P.J., Czymzik, M., Hübener, T., Stadmark, J., Dellwig, O., Roeser, P., Conley, D.J., 2021. Human influence on the continental Si budget during the last 4300 years: δ30Sidiatom in varved lake sediments (Tiefer See, NE Germany). Quat. Sci. Rev. 258, 106869. https://doi.org/10.1016/j.quascirev.2021.106869.

Nantke, C.K., Frings, P.J., Stadmark, J., Czymzik, M., Conley, D.J., 2019. Si cycling in transition zones: a study of Si isotopes and biogenic silica accumulation in the Chesapeake Bay through the Holocene. Biogeochemistry 146, 145–170. https://doi.org/10.1007/s10533-019-00618-w.

Niessen, F., Gebhardt, A.C., Kuhn, G., Magens, D., Monien, D., 2013. Porosity and density of the AND-1B sediment core, McMurdo Sound region, Antarctica: field consolidation enhanced by grounded ice. Geosphere 9, 489. https://doi.org/10.1130/GES00704.1.

Opfergelt, S., Delmelle, P., 2012. Silicon isotopes and continental weathering processes: assessing controls on Si transfer to the ocean. C. R. Géosci. 344, 723–738. https://doi.org/10.1016/j.crte.2012.09.006.

Opfergelt, S., Eiriksdottir, E.S., Burton, K.W., Einarsson, A., Siebert, C., Gislason, S.R., Halliday, A.N., 2011. Quantifying the impact of freshwater diatom productivity on

silicon isotopes and silicon fluxes: Lake Myvatn, Iceland. Earth Planet. Sci. Lett. 305, 73–82. https://doi.org/10.1016/j.epsl.2011.02.043.

Panizzo, V., Roberts, S., Swann, G.E., McGowan, S., Mackay, A.W., Vologina, E., Pashley, V., Horstwood, M.S., 2018. Spatial differences in dissolved silicon utilization in Lake Baikal, Siberia: examining the impact of high diatom biomass events and eutrophication. Limnol. Oceanogr. 63, 1562–1578. https://doi.org/10.1002/lno.10792.

Panizzo, V.N., Swann, G.E.A., Mackay, A.W., Vologina, E., Alleman, L., André, L., Pashley, V.H., Horstwood, M.S.A., 2017. Constraining Modern-Day Silicon Cycling in Lake Baikal. AGU Publications, pp. 556–574.

Panizzo, V.N., Swann, G.E.A., Mackay, A.W., Vologina, E., Sturm, M., Pashley, V., Horstwood, M.S.A., 2016. Insights into the transfer of silicon isotopes into the sediment record. Biogeosciences 13, 147–157. https://doi.org/10.5194/bg-13-147-2016.

Psenner, R., 1989. Chemistry of high mountain lakes in siliceous chatchments of the Central Eastern Alps. Aquat. Sci. 51, 108–128. https://doi.org/10.1007/bf00879298.

Reynolds, B.C., Aggarwal, J., Andre, L., Baxter, D., Beucher, C., Brzezinski, M.A., Engstrom, E., Georg, R.B., Land, M., Leng, M.J., Opfergelt, S., Rodushkin, I., Sloane, H.J., van den Boorn, S.H.J.M., Vroon, P.Z., Cardinal, D., 2007. An inter-laboratory comparison of Si isotope reference materials. J. Anal. At. Spectrom. 22, 561–568. https://doi.org/10.1039/b616755a.

Richter, F.M., Turekian, K.K., 1993. Simple models for the geochemical response of the ocean to climatic and tectonic forcing. Earth Planet. Sci. Lett. 119, 121–131. https://doi.org/10.1016/0012-821x(93)90010-7.

Schiller, C.M., 2020. Hydrothermal Influences on the Holocene Environmental History of Central Yellowstone National Park. PhD thesis. Montana State University. https://scholarworks.montana.edu/xmlui/bitstream/handle/1/16052/schiller-hydrothermal-2020.pdf?sequence=1.

Schiller, C.M., Whitlock, C., Alt, M., Morgan, L.A., 2020a. Vegetation responses to Quaternary volcanic and hydrothermal disturbances in the Northern Rocky Mountains and Greater Yellowstone Ecosystem (USA). Palaeogeogr. Palaeoclimatol. Palaeoecol. https://doi.org/10.1016/j.palaeo.2020.109859.

Schiller, C.M., Whitlock, C., Brown, S.R., 2022. Holocene geo-ecological evolution of Lower Geyser Basin, Yellowstone National Park (USA). Quat. Res. 105, 201–217. https://doi.org/10.1017/qua.2021.42.

Schiller, C.M., Whitlock, C., Elder, K.L., Iverson, N.A., Abbott, M.B., 2020b. Erroneously old radiocarbon ages from terrestrial pollen concentrates in Yellowstone Lake, Wyoming, USA. Radiocarbon, 1–22. https://doi.org/10.1017/rdc.2020.118.

Schmidtbauer, K., Noble, P., Rosen, M., Conley, D.J., Frings, P.J., 2022. Linking silicon isotopic signatures with diatom communities. Geochim. Cosmochim. Acta 323, 102–122. https://doi.org/10.1016/j.gca.2022.02.015.

Scribner, A.M., Kurtz, A.C., Chadwick, O.A., 2006. Germanium sequestration by soil: targeting the roles of secondary clays and fe-oxyhydroxides. Earth Planet. Sci. Lett. 243, 760–770. https://doi.org/10.1016/j.epsl.2006.01.051.

Shanks, W.C., Alt, J.C., Morgan, L.A., 2007. Geochemistry of sublacustrine hydrothermal deposits in Yellowstone Lake - hydrothermal reactions, stable-isotope systematics, sinter deposition, and spire formation. In: Publications of the US Geological Survey. https://digitalcommons.unl.edu/usgspubs/85.

Shemesh, A., Mortlock, R., Froelich, P., 1989. Late Cenozoic Ge/Si record of marine biogenic opal: implications for variations of riverine fluxes to the ocean. Paleoceanography 4, 221–234. https://doi.org/10.1029/pa004i003p00221.

Stauffer, R.E., Thompson, J.M., 1984. Arsenic and antimony in geothermal waters of Yellowstone National Park, Wyoming, USA. Geochim. Cosmochim. Acta 48, 2547–2561. https://doi.org/10.1016/0016-7037(84)90305-3.

Street-Perrott, F.A., Barker, P.A., Leng, M.J., Sloane, H.J., Wooller, M.J., Ficken, K.J., Swain, D.L., 2008. Towards an understanding of late Quaternary variations in the continental biogeochemical cycle of silicon: multi-isotope and sediment-flux data for Lake Rutundu, Mt Kenya, East Africa, since 38 ka BP. J. Quat. Sci. 23, 375–387. https://doi.org/10.1002/jqs.1187. published for the Quaternary Research Association.

Strickland, J., Parsons, T., 1972. A Practical Handbook of Seawater Analysis, 2nd ed. Bulletin, vol. 167. The Alger Press Ltd. https://epic.awi.de/id/eprint/39262/1/Strickland-Parsons_1972.pdf. Journal of the Fisheries Research Board of Canada, Ottawa.

Struyf, E., Mörth, C.M., Humborg, C., Conley, D.J., 2010. An enormous amorphous silica stock in boreal wetlands. J. Geophys. Res., Biogeosci. 115, G04008. https://doi.org/10.1029/2010jg001324.

Sun, X., Andersson, P., Land, M., Humborg, C., Mörth, C.M., 2010. Stable silicon isotope analysis on nanomole quantities using MC-ICP-MS with a hexapole gas-collision cell. J. Anal. At. Spectrom. 25, 156–162. https://doi.org/10.1039/B911113A.

Sutton, J., Ellwood, M.J., Maher, William A., Croot, P.L., 2010. Oceanic distribution of inorganic germanium relative to silicon: germanium discrimination by diatoms. Glob. Biogeochem. Cycles 24, GB2017. https://doi.org/10.1029/2009gb003689.

Sutton, J.N., André, L., Cardinal, D., Conley, D.J., De Souza, G.F., Dean, J., Dodd, J., Ehlert, C., Ellwood, M.J., Frings, P.J., et al., 2018. A review of the stable isotope bio-geochemistry of the global silicon cycle and its associated trace elements. Front. Earth Sci. 5. https://doi.org/10.3389/feart.2017.00112.

Sutton, J.N., Varela, D.E., Brzezinski, M.A., Beucher, C.P., 2013. Species-dependent silicon isotope fractionation by marine diatoms. Geochim. Cosmochim. Acta 104, 300–309. https://doi.org/10.1016/j.gca.2012.10.057.

Swann, G.E., Leng, M.J., Juschus, O., Melles, M., Brigham-Grette, J., Sloane, H.J., 2010. A combined oxygen and silicon diatom isotope record of Late Quaternary change in Lake El'gygytgyn, North East Siberia. Quat. Sci. Rev. 29, 774–786. https://doi.org/10.1016/j.quascirev.2009.11.024.

Taylor, A., Blum, J.D., 1995. Relation between soil age and silicate weathering rates determined from the chemical evolution of a glacial chronosequence. Geology 23, 979. https://doi.org/10.1130/0091-7613(1995)023<0979:RBSAAS>2.3.CO;2. https://pubs.geoscienceworld.org/geology/article/23/11/979-982/190025.

Theriot, E.C., Fritz, S.C., Whitlock, C., Conley, D.J., 2006. Late Quaternary rapid morphological evolution of an endemic diatom in Yellowstone Lake, Wyoming. Paleobiology 32, 38–54. https://doi.org/10.1666/02075.1.

Tiller, C.C., 1995. Postglacial sediment stratigraphy of large lakes in Greater Yellowstone: Scenarios of tectonic and climatic forcing. Master's thesis. University of Minnesota.

Treguer, P., Nelson, D.M., Van Bennekom, A.J., DeMaster, D.J., Leynaert, A., Queguiner, B., 1995. The silica balance in the world ocean: a reestimate. Science 268, 375–379. https://doi.org/10.1126/science.268.5209.375.

Tréguer, P.J., De La Rocha, C.L., 2013. The world ocean silica cycle. Annu. Rev. Mar. Sci. 5, 477–501. https://doi.org/10.1146/annurev-marine-121211-172346.

Tribovillard, N., 2013. The Ge/Si ratio as a tool to recognize biogenic silica in chert. C. R. Géosci. 345, 160–165. https://doi.org/10.1016/j.crte.2013.02.005.

Tréguer, P.J., Sutton, J.N., Brzezinski, M., Charette, M.A., Devries, T., Dutkiewicz, S., Ehlert, C., Hawkings, J., Leynaert, A., Liu, S.M., Llopis Monferrer, N., López-Acosta, M., Maldonado, M., Rahman, S., Ran, L., Rouxel, O., 2021. Reviews and syntheses: the biogeochemical cycle of silicon in the modern ocean. Biogeosciences 18, 1269–1289. https://doi.org/10.5194/bg-18-1269-2021.

Tudor, A., Fowler, A., Foustoukos, D.I., Moskowitz, B., Wang, L., Tan, C., Seyfried, W.E., 2021. Geochemistry of vapor-dominated hydrothermal vent deposits in Yellowstone Lake, Wyoming. J. Volcanol. Geotherm. Res. 414, 107231. https://doi.org/10.1016/j.jvolgeores.2021.107231.

Varela, D.E., Pride, C.J., Brzezinski, M.A., 2004. Biological fractionation of silicon isotopes in Southern Ocean surface waters. Glob. Biogeochem. Cycles 18, GB1047. https://doi.org/10.1029/2003gb002140.

Von Blanckenburg, F., Schuessler, J.A., Bouchez, J., Frings, P.J., Uhlig, D., Oelze, M., Frick, D.A., Hewawasam, T., Dixon, J., Norton, K., 2021. Rock weathering and nutrient cycling along an erodosequence. Am. J. Sci. 321, 1111–1163. https://doi.org/10.2475/08.2021.01.

Wang, B., Liu, C.Q., Maberly, S.C., Wang, F., Hartmann, J., 2016. Coupling of carbon and silicon geochemical cycles in rivers and lakes. Sci. Rep. 6, 35832. https://doi.org/10.1038/srep35832.

Westacott, S., Planavsky, N.J., Zhao, M.Y., Hull, P.M., 2021. Revisiting the sedimentary record of the rise of diatoms. Proc. Natl. Acad. Sci. USA 118, e2103517118. https://doi.org/10.1073/pnas.2103517118.

Whitlock, C., 1993. Postglacial vegetation and climate of Grand Teton and southern Yellowstone National Parks. Ecol. Monogr. 63, 173–198. https://doi.org/10.2307/2937179.

Whitlock, C., Dean, W.E., Fritz, S.C., Stevens, L.R., Stone, J.R., Power, M.J., Rosenbaum, J.R., Pierce, K.L., Bracht-Flyr, B.B., 2012. Holocene seasonal variability inferred from multiple proxy records from Crevice Lake, Yellowstone National Park, USA. Palaeogeogr. Palaeoclimatol. Palaeoecol. 331, 90–103. https://doi.org/10.1016/j.palaeo.2012.03.001.

Yeghicheyan, D., Aubert, D., Bouhnik-Le Coz, M., Chmeleff, J., Delpoux, S., Djouraev, I., Granier, G., Lacan, F., Piro, J., Rousseau, T., Cloquet, C., Marquet, A., Menniti, C., Pradoux, C., Freydier, R., Vieira Da Silva-Filho, E., Suchorski, K., 2019. A new interlaboratory characterisation of silicon, rare Earth elements and twenty-two other trace element concentrations in the natural river water certified reference material SLRS-6 (NRC-CNRC). Geostand. Geoanal. Res. 43, 475–496. https://doi.org/10.1111/ggr.12268.

Yeghicheyan, D., Bossy, C., Le Bouhnik, Coz M., Douchet, C., Granier, G., Heimburger, A., Lacan, F., Lanzanova, A., Rousseau, T.C., Seidel, J.L., et al., 2013. A compilation of silicon, rare earth element and twenty-one other trace element concentrations in the natural river water reference material SLRS-5 (NRC-CNRC). Geostand. Geoanal. Res. 37, 449–467. https://doi.org/10.1111/j.1751-908x.2013.00232.x.

Zahajská, P., Cartier, R., Fritz, S.C., Stadmark, J., Opfergelt, S., Yam, R., Shemesh, A., Conley, D.J., 2021. Impact of Holocene climate change on silicon cycling in Lake 850, Northern Sweden. Holocene 31, 1582–1592. https://doi.org/10.1177/09596836211025973.

Zhang, A., Zhang, J., Zhang, R., Xue, Y., 2014. Modified enrichment and purification protocol for dissolved silicon-isotope determination in natural waters. J. Anal. At. Spectrom. 29, 2414–2418. https://doi.org/10.1039/C4JA00122B.

Zhou, J., Bing, H., Wu, Y., Yang, Z., Wang, J., Sun, H., Luo, J., Liang, J., 2016. Rapid weathering processes of a 120-year-old chronosequence in the Hailuogou Glacier foreland, Mt. Gongga, SW China. Geoderma 267, 78–91. https://doi.org/10.1016/j.geoderma.2015.12.024.

Ziegler, K., Chadwick, O.A., Brzezinski, M.A., Kelly, E.F., 2005. Natural variations of δ^{30}Si ratios during progressive basalt weathering, Hawaiian Islands. Geochim. Cosmochim. Acta 69, 4597–4610. https://doi.org/10.1016/j.gca.2005.05.008.